

First full-shape joint analysis of the two- and three-point correlation functions on real data: Λ CDM cosmological constraints from BOSS DR12

M. Guidi^{*1,2}, M. Moresco^{1,2}, A. Veropalumbo^{3,4,5}, L. Cavazzini¹, A. Farina^{3,4}, and A. Labate^{1,2}

¹ Dipartimento di Fisica e Astronomia, Università di Bologna, Via Gobetti 93/2, 40129 Bologna, Italy

² INAF–Osservatorio di Astrofisica e Scienza dello Spazio di Bologna, Via Piero Gobetti 93/3, I-40129 Bologna, Italy

³ INAF–Osservatorio Astronomico di Brera, Via Brera 28, I-20122 Milano, Italy

⁴ INFN–Sezione di Genova, Via Dodecaneso 33, 16146 Genova, Italy

⁵ Dipartimento di Fisica, Università di Genova, Via Dodecaneso 33, 16146 Genova, Italy

June 26, 2026

ABSTRACT

The three-point correlation function (3PCF) encodes cosmological information beyond the two-point correlation function (2PCF), yet a full-shape joint analysis in redshift space using real data has so far been lacking. In this work, we present the first full-shape cosmological constraints from a joint analysis of 2PCF and 3PCF in redshift space, using BOSS DR12 data, extending to real data, including Alcock–Paczyński and redshift space distortions, the full-shape configuration-space framework validated in real space for the first time by [Euclid Collaboration: Guidi et al. \(2026\)](#). We model both statistics adopting the velocity difference generating function (VDG) framework, incorporating non-perturbative Fingers-of-God damping, a complete Eulerian galaxy bias expansion, and infrared resummation. Fast and accurate theoretical predictions are obtained using dedicated emulators, which enable a full-shape likelihood analysis of the 3PCF and its combination with the 2PCF, varying the cosmological parameters $10^9 A_s$, ω_{cdm} and h , while the baryon fraction density ω_b is fixed to its fiducial value. The covariance matrix is estimated from 2048 MultiDark-Patchy mocks, and an optimal data-vector compression ensures a stable covariance inversion. The perturbative model is validated against goodness-of-fit tests and posterior stability diagnostics across different scales, and provides a good description of the joint data vector down to $r_{\text{min}}^{3\text{PCF}} \sim 60 h^{-1} \text{Mpc}$. We find that the joint 2PCF+3PCF analysis yields significant improvements over the 2PCF-only baseline, with gains of approximately 29%, 10%, and 24% on $\sigma(h)$, $\sigma(\omega_{\text{cdm}})$, and $\sigma(A_s)$, respectively. The improvements found in this analysis mainly arise from the BAO cosmological information encoded in the 3PCF triangle configurations, which brings additional information with respect to the 2PCF alone.

Key words. Cosmology:large-scale-structure, theory, galaxy survey, galaxy bias, cosmological parameters, 3-point statistics

1. Introduction

Galaxy clustering has emerged as one of the most powerful probes of the large-scale structure (LSS) of the Universe, offering a direct window onto the statistical properties of the matter and galaxy density field across a wide range of scales and cosmic epochs. Over the past two decades, spectroscopic surveys such as the Baryon Oscillation Spectroscopic Survey (BOSS; [Dawson et al. 2013](#); [Alam et al. 2017](#)), the Dark Energy Spectroscopic Instrument (DESI; [DESI Collaboration et al. 2016](#)) and *Euclid* ([Euclid Collaboration: Mellier et al. 2025](#)) have mapped and are still mapping the three-dimensional distribution of millions of galaxies, enabling precise measurements of the two-point correlation function (2PCF) and its Fourier-space counterpart, the power spectrum. These measurements have been exploited to use baryon acoustic oscillations (BAOs) as a standard ruler to reconstruct the background expansion history ([Seo & Eisenstein 2003](#); [Eisenstein et al. 2005](#); [Beutler et al. 2014](#); [Ross et al. 2007](#); [Adame et al. 2025a](#)). They have also been used to probe the growth of cosmic structures through redshift-space distortions (RSD; [Peacock et al. 2001](#); [Guzzo et al. 2008](#); [Beutler et al. 2017b](#); [Sánchez et al. 2017b](#)), as

well as through full-shape analyses of their redshift-space multipoles ([Sánchez et al. 2013](#); [D’Amico et al. 2020](#); [Ivanov et al. 2020](#); [Philcox & Ivanov 2022](#)).

While two-point statistics are sufficient to characterise a Gaussian random field, the observed galaxy density field deviates significantly from Gaussianity. This non-Gaussian character arises from multiple sources: the nonlinear evolution of density perturbations ([Fry 1984](#); [Bernardeau et al. 2002](#)), the non-linear and non-local relation between galaxies and the underlying matter field (galaxy bias; [Fry & Gaztañaga 1993](#); [Fry 1994](#); [Chan et al. 2012](#); [Baldauf et al. 2012](#); [Eggemeier et al. 2019](#)), and redshift space distortions (RSD) ([Hivon et al. 1995](#); [Scoccimarro et al. 1999](#)). Additionally, primordial non-Gaussianities, potentially generated during inflation, can leave detectable imprints on the large-scale galaxy distribution ([Verde et al. 2000](#); [Scoccimarro 2000](#); [Scoccimarro et al. 2004](#)). All these effects transfer cosmologically relevant information from the two-point to higher-order statistics, in particular to the three-point correlation function (3PCF) in configuration space and the bispectrum in Fourier space. The joint analysis of two- and three-point statistics has been shown to break parameter degeneracies and significantly tighten cosmological constraints (see e.g. [Sefusatti & Komatsu](#)

* e-mail: massimo.guidi6@unibo.it

2007; Moresco et al. 2014, 2017; D’Amico et al. 2020; Philcox & Ivanov 2022; D’Amico et al. 2025; Cabass et al. 2022; Veropalumbo et al. 2021; Kuruvilla & Porciani 2020; Moradinezhad Dizgah et al. 2021; Farina et al. 2026; Pugno et al. 2025; Euclid Collaboration: Guidi et al. (2026).

The majority of full-shape analyses exploiting three-point statistics have so far focused on the bispectrum in Fourier space (Gil-Marín et al. 2017; D’Amico et al. 2020, 2025; Cabass et al. 2022; Philcox & Ivanov 2022; Adame et al. 2025a; Novell-Masot et al. 2025, 2026; Forero-Sánchez et al. 2026). The preference for Fourier space is driven by the availability of efficient estimators and well-developed perturbation theory (PT) frameworks, including Eulerian SPT and Lagrangian PT (Bernardeau et al. 2002; Matsubara 2008b,a; Carlson et al. 2013; Wang et al. 2014), and the effective field theory of large-scale structure (EFTofLSS; Baumann et al. 2012; Carrasco et al. 2012). Configuration-space analyses, on the other hand, offer a natural advantage in handling the complex geometry of spectroscopic surveys: the Szapudi–Szalay estimator (Szapudi & Szalay 1998) automatically accounts for boundary and selection effects, avoiding the need to convolve theoretical models with survey window functions. The main obstacles to exploiting the 3PCF have historically been the $O(N^3)$ computational cost of direct triplet counting and the limited availability of accurate redshift-space models. The introduction of a spherical harmonic decomposition estimator (Slepian & Eisenstein 2015, 2018) reduced the computational scaling to $O(N^2)$, enabling the analysis of catalogues with $N \sim O(10^7)$ galaxies, and triggered a rapid development of independent measurement tools (Marulli et al. 2016; Farina et al. 2026; Euclid Collaboration: Veropalumbo et al. 2026; Philcox et al. 2021b). This progress culminated in the first detection of the BAO peak in the galaxy 3PCF BOSS data (Slepian et al. 2017), DESI data (Kamalnejad et al. 2026) and cluster of galaxies (Moresco et al. 2021), as well as joint 2PCF+3PCF analyses for the measurement of the linear growth rate of cosmic structures, as shown in Veropalumbo et al. (2021).

Advances in 3PCF estimation have driven parallel progress in theoretical modelling. Perturbative predictions at leading (LO) next-to-leading (NLO) orders for the real-space 3PCF, incorporating non-local bias and infrared (IR) resummation, have been validated against N -body simulations and synthetic galaxy catalogues (Veropalumbo et al. 2022; Guidi et al. 2023). Euclid Collaboration: Guidi et al. (2026) extended this modelling framework for the first time to a full-shape joint 2PCF+3PCF analysis in real space on catalogues mimicking the *Euclid* spectroscopic sample, demonstrating that perturbative models can accurately recover cosmological parameters from configuration-space data. However, a complete extension to redshift-space data has remained a critical missing step, primarily due to the absence of accurate and efficient theoretical predictions for the redshift-space 3PCF suitable for full-shape likelihood analyses.

In this paper, we present the first full-shape joint analysis of the 2PCF and 3PCF multipoles in redshift space using BOSS DR12 data (Alam et al. 2017), splitting the sample into two effective redshift bins, *low- z* ($\bar{z} \simeq 0.38$) and *high- z* ($\bar{z} \simeq 0.61$), obtained via redshift resampling of the original LOWZ and CMASS galaxy samples.

The theoretical model is built on the velocity-difference generating function (VDG) framework (Eggemeier et al. 2025), which provides a non-perturbative treatment of LOS velocity statistics and their damping effects, combined with a one-loop SPT description of the density field and a complete galaxy

bias expansion including non-local and higher-derivative terms. The Infrared resummation is implemented following Blas et al. (2016) to accurately capture the BAO feature in both statistics. Together, these ingredients constitute a complete perturbative model for the configuration-space galaxy clustering signal, directly applicable to upcoming Stage IV surveys.

This paper is organised as follows. In Sect. 2 we introduce the theoretical framework, including the definitions of the 2PCF and 3PCF multipoles, the VDG model, the galaxy bias expansion, and IR resummation. Section 3 describes the BOSS DR12 data, the mock catalogues used for covariance estimation while the estimators and the clustering measurements are given in Appendix B.1. Section 4 details the likelihood and inference setup. Finally, our results are presented in Sects. 5, 5.2, where we discuss the full-shape constraints on cosmological and bias parameters from the 2PCF alone and from the joint 2PCF+3PCF analysis. We draw our conclusions in Sect. 6.

2. Theoretical models

2.1. The velocity difference generating function framework

In spectroscopic galaxy surveys, the line-of-sight positions of galaxies are inferred from their redshifts, which include a contribution from peculiar velocities in addition to the Hubble flow. This induces a systematic displacement of galaxies along the line of sight in the inferred coordinate frame, the so-called redshift-space distortions (RSD), which must be carefully modelled to extract unbiased cosmological information from the observed clustering signal. In the distant-observer, plane-parallel approximation, the mapping from real-space positions \mathbf{x} to redshift-space positions \mathbf{s} is written as

$$\mathbf{s} = \mathbf{x} + f u_{\hat{\mathbf{n}}}(\mathbf{x}) \hat{\mathbf{n}}, \quad (1)$$

where $f \equiv d \ln D / d \ln a$ is the logarithmic growth rate, D is the linear growth factor, $\hat{\mathbf{n}}$ denotes the (fixed) LOS, and the LOS velocity field is expressed as $v_{\hat{\mathbf{n}}}(\mathbf{x}) = f \mathcal{H} u_{\hat{\mathbf{n}}}(\mathbf{x})$ with \mathcal{H}^{-1} the comoving Hubble scale.

The Fourier-space galaxy density contrast in redshift space can be written exactly as (Eggemeier et al. 2025)

$$\delta_s(\mathbf{k}) = \int_{\mathbf{x}} e^{i\mathbf{k}\cdot\mathbf{x}} e^{\lambda u_{\hat{\mathbf{n}}}(\mathbf{x})} [\delta_g(\mathbf{x}) + f \partial_{\hat{\mathbf{n}}} u_{\hat{\mathbf{n}}}(\mathbf{x})], \quad (2)$$

where we introduced the shorthand $\lambda \equiv i f k_{\hat{\mathbf{n}}}$, and the term in square brackets reduces to the Kaiser limit at large scales when the exponential is set to unity. Here δ_g denotes the galaxy overdensity field, which encodes the non-linear and non-local relation between the observed galaxy distribution and the underlying matter field through a galaxy bias expansion; the explicit parametrisation adopted in this work is introduced in Sect. 2.2.

A conventional approach is to expand the exponential in Eq. (2) and express δ_s in terms of redshift-space PT kernels Z_n ,

$$\delta_s(\mathbf{k}) = \sum_{n=1}^{\infty} \int_{\mathbf{q}_1} \cdots \int_{\mathbf{q}_n} (2\pi)^3 \delta_{\mathbf{D}}(\mathbf{k} - \mathbf{q}_{1\dots n}) Z_n(\mathbf{q}_1, \dots, \mathbf{q}_n) \times \delta_{\text{lin}}(\mathbf{q}_1) \cdots \delta_{\text{lin}}(\mathbf{q}_n), \quad (3)$$

which yields the familiar SPT expressions for P_s and B_s when truncating at a fixed order in perturbations. For a detailed description of PT kernels, see Appendix A.3.

In this work, we instead exploit that the mapping in Eq. (2) allows an exact reformulation of the two- and three-point statistics in terms of configuration-space correlators involving exponentials of velocity differences. In particular, for the power spectrum one can write (Eggemeier et al. 2025)

$$P_s(\mathbf{k}) = \int d^3r e^{i\mathbf{k}\cdot\mathbf{r}} \langle e^{\lambda\Delta u_z} D(\mathbf{x}) D(\mathbf{x}') \rangle \quad (4)$$

where $\Delta u \equiv u_{\hat{n}}(\mathbf{x}) - u_{\hat{n}}(\mathbf{x}')$, $\mathbf{r} \equiv \mathbf{x} - \mathbf{x}'$ and $D \equiv \delta_g + f \partial_{\hat{n}} u_{\hat{n}}$ collects the Kaiser-limit density contribution but evaluated using fully non-linear fields

Applying a cumulant expansion to the correlator in Eq. (4) yields an exact separation

$$\langle e^{\lambda\Delta u_z} D D' \rangle = W(\lambda, \mathbf{r}) \langle e^{\lambda\Delta u_z} D D' \rangle_c, \quad (5)$$

and

$$W(\lambda, \mathbf{r}) \equiv \langle e^{\lambda\Delta u_z} \rangle = \exp[\langle e^{\lambda\Delta u_z} \rangle_c], \quad (6)$$

where $\langle \dots \rangle_c$ denotes a connected correlator. The prefactor W is the *velocity-difference generating function* (VDG): successive derivatives of $\ln W$ with respect to λ generate the cumulants of LOS velocity differences and thus control the non-Gaussian damping associated with Fingers-of-God. The key modelling choice is to treat W as a prescribed, non-perturbative function rather than expanding it as a power series in λ , which would revert to the standard redshift-space PT expansion.

On large scales, the dominant impact of the VDG is well approximated by its infinite-separation limit, where it depends only on λ and not on \mathbf{r} . In this approximation the two-point VDG becomes

$$W(\lambda, \mathbf{r}) \simeq W^P(\lambda) = \frac{1}{\sqrt{1 + \frac{1}{2} a_{\text{vir}}^2 \lambda^2}} \exp\left[\frac{\lambda^2 \sigma_v^2}{1 + \frac{1}{2} a_{\text{vir}}^2 \lambda^2}\right], \quad (7)$$

where a_{vir} is a free parameter controlling the kurtosis contribution to the LOS velocity-difference statistics, and $\sigma_v^2 \equiv \langle u_z^2 \rangle$ is the (bulk-flow) velocity dispersion. In linear theory, σ_v^2 is computed from the velocity divergence power spectrum (or equivalently P_{lin}) as

$$\sigma_v^2 = \frac{1}{3} \int \frac{d^3q}{(2\pi)^3} \frac{P_{\text{lin}}(q)}{q^2}. \quad (8)$$

For the bispectrum, an analogous manipulation yields expressions involving a three-point VDG, $W_{1,2}(\mathbf{r}_{13}, \mathbf{r}_{23}) \equiv \langle e^{\lambda_1 u_{13,z} + \lambda_2 u_{23,z}} \rangle$. In the infinite-separation approximation we adopt

$$\begin{aligned} W_{1,2}(\mathbf{r}_{13}, \mathbf{r}_{23}) &\simeq W^B(\lambda_1, \lambda_2, \lambda_3) \\ &= \frac{1}{\left(1 + \frac{1}{2} a_{\text{vir}}^2 \lambda_{123}^2\right)^{3/2}} \exp\left[\frac{\lambda_{123}^2 \sigma_v^2}{1 + \frac{1}{2} a_{\text{vir}}^2 \lambda_{123}^2}\right] \end{aligned} \quad (9)$$

where $\lambda_i \equiv i f k_{i,z}$ and $\lambda_{123}^2 \equiv \lambda_1^2 + \lambda_2^2 + \lambda_3^2$ (with $\mathbf{k}_1 + \mathbf{k}_2 + \mathbf{k}_3 = \mathbf{0}$ for closed triangles).

2.2. Perturbative expansion

Having isolated the VDG contribution, all remaining terms in the cumulant-expanded expressions (i.e. the connected correlators in Eq. (6)) are treated perturbatively. Concretely, we model the deterministic clustering contributions using perturbation theory for the matter and velocity fields, together with an Eulerian galaxy

bias expansion. We adopt the standard EFT bias basis used in Eggemeier et al. (2025), writing the galaxy overdensity as

$$\begin{aligned} \delta_g(\mathbf{x}) &= b_1 \delta(\mathbf{x}) + \frac{b_2}{2} \delta^2(\mathbf{x}) + b_{\nabla^2} \nabla^2 \delta(\mathbf{x}) \\ &\quad + b_{\mathcal{G}_2} \mathcal{G}_2(\Phi_v | \mathbf{x}) + b_{\Gamma_3} \Gamma_3(\mathbf{x}), \end{aligned} \quad (10)$$

where \mathcal{G}_2 and Γ_3 are non-local operators, defined as

$$\mathcal{G}_2(\Phi | \mathbf{x}) := [\partial_i \partial_j \Phi(\mathbf{x})]^2 - [\partial^2 \Phi(\mathbf{x})]^2, \quad (11)$$

$$\Gamma_3(\mathbf{x}) := \mathcal{G}_2(\Phi | \mathbf{x}) - \mathcal{G}_2(\Phi_v | \mathbf{x}), \quad (12)$$

and $\Phi(\mathbf{x})$ and $\Phi_v(\mathbf{v})$ represent the gravitational and velocity potential. where δ is the matter overdensity and \mathcal{G}_2 denotes the Galilean-invariant tidal operator, while b_{∇^2} is the leading higher-derivative bias parameter capturing spatial non-locality.

2.3. Modelling the redshift-space power spectrum and two-point correlation function

The configuration-space multipoles of the 2PCF are related to the power spectrum multipoles via the Hankel transform

$$\xi_{s,\ell}(r) = i^\ell \int \frac{dk}{2\pi^2} k^2 j_\ell(kr) P_{s,\ell}(k). \quad (13)$$

The VDG model for the redshift-space galaxy power spectrum can be written schematically as

$$P_s^{\text{VDG}}(\mathbf{k}) = W^P(\mathbf{k}) \left[P_s^{\text{tree}}(\mathbf{k}) + P_s^{1\text{-loop}}(\mathbf{k}) + P_s^{\text{ctr}}(\mathbf{k}) \right] + \Delta P(\mathbf{k}), \quad (14)$$

where W^P is the two-point VDG damping function (in the infinite-separation approximation), and

$$P_s^{\text{tree}}(\mathbf{k}) = Z_1^2(\mathbf{k}) P_{\text{lin}}(k), \quad (15)$$

$$\begin{aligned} P_s^{1\text{-loop}}(\mathbf{k}) &= P_{s,22}(k) + P_{s,13}(k) \\ &= 2 \int_{\mathbf{q}} Z_2^2(\mathbf{q}, \mathbf{k} - \mathbf{q}) P_{\text{lin}}(|\mathbf{k} - \mathbf{q}|) P_{\text{lin}}(q) \\ &\quad + 6 Z_1(\mathbf{k}) P_{\text{lin}}(k) \int_{\mathbf{q}} Z_3(\mathbf{q}, -\mathbf{q}, \mathbf{k}) P_{\text{lin}}(q), \end{aligned} \quad (16)$$

$$P_s^{\text{ctr}}(k, \mu) = -2 k^2 P_{\text{lin}}(\mathbf{k}) \sum_{n=0}^2 c_{2n} \mathcal{L}_{2n}(\mu), \quad (17)$$

$$\Delta P(\mathbf{k}) = -\frac{\lambda^2}{2} \sigma_v^2 P_{DD}(k) + \frac{\lambda^2}{2} \int_{\mathbf{q}} \frac{q_z^2}{q^4} P_{\theta\theta}(q) P_{DD}(|\mathbf{k} - \mathbf{q}|). \quad (18)$$

Stochastic contributions are analytic in k^2 in Fourier space: a constant shot-noise term maps in configuration space to a Dirac delta function $\delta^{(3)}(\mathbf{r})$, terms proportional to k^2 map to its Laplacian $\nabla^2 \delta^{(3)}(\mathbf{r})$, and higher-order terms in k^{2n} to its higher spatial derivatives. In all cases, these contributions are localised at vanishing separation and do not affect the correlation functions at finite separations within the EFT regime of validity.

2.4. Modelling the redshift-space bispectrum and three-point correlation function

The corresponding configuration-space multipoles of the 3PCF are related to the bispectrum multipoles via

$$\zeta_\ell(r_{12}, r_{13}) = (-1)^\ell \int \frac{dk_1 dk_2}{(2\pi)^6} k_1^2 k_2^2 B_\ell(k_1, k_2) j_\ell(k_1 r_{12}) j_\ell(k_2 r_{13}), \quad (19)$$

which is evaluated efficiently using 2D-FFTLog-based algorithms (e.g. Fang et al. 2020; Umeh 2021; Guidi et al. 2023; Farina et al. 2026; Pugno et al. 2025). At leading (tree) order in PT, the VDG model for the bispectrum takes the form (Eggemeier et al. 2025)

$$B_s^{\text{VDG}}(\mathbf{k}_1, \mathbf{k}_2, \mathbf{k}_3) = W^B(\mathbf{k}_1, \mathbf{k}_2, \mathbf{k}_3) B^{\text{tree}}(\mathbf{k}_1, \mathbf{k}_2, \mathbf{k}_3), \quad (20)$$

where W^B is the three-point VDG damping function in the infinite-separation approximation, and B^{tree} is the standard SPT tree-level redshift-space galaxy bispectrum (Ivanov & Sibiryakov 2018),

$$B^{\text{tree}}(\mathbf{k}_1, \mathbf{k}_2, \mathbf{k}_3) = 2 Z_1(\mathbf{k}_1) Z_1(\mathbf{k}_2) Z_2(\mathbf{k}_1, \mathbf{k}_2) P_{\text{lin}}(k_1) P_{\text{lin}}(k_2) + \text{cyc.} \quad (21)$$

where cyc. denotes cyclic permutations of $(\mathbf{k}_1, \mathbf{k}_2, \mathbf{k}_3)$. The stochastic contributions to the bispectrum are analytic in k^2 in Fourier space: a constant shot-noise term maps in configuration space to a Dirac delta function localised at coincident points, terms proportional to k^2 to its Laplacian, and higher-order terms in k^{2n} to higher spatial derivatives. In all cases, these contributions are non-zero only when two or more vertices of the triangle collapse to the same position. Since in practice the 3PCF is measured only at finite, non-zero separations, these contributions never enter the analysis and can therefore be safely neglected.

2.5. IR resummation

To account for the smearing of the BAO feature induced by large-scale displacements, we implement infrared (IR) resummation in the wiggle/no-wiggle approach (Eisenstein et al. 2007; Smith et al. 2007; Crocce & Scoccimarro 2008; Matsubara 2008b; Desjacques et al. 2010; Baldauf et al. 2015; Senatore & Zaldarriaga 2015). The linear power spectrum is decomposed as $P_{\text{lin}}(k) = P_{\text{nw}}(k) + P_{\text{w}}(k)$, and only the oscillatory component is damped,

$$P_{\text{lin,IR}}(k) = P_{\text{nw}}(k) + e^{-k^2 \Sigma_{\text{tot}}^2} P_{\text{w}}(k). \quad (22)$$

In redshift space the displacement variance depends on the line-of-sight direction and reads

$$\Sigma_{\text{tot}}^2(\mu) = (1 + f\mu^2)^2 \Sigma_1^2 + f^2 \mu^2 (1 - \mu^2) \Sigma_2^2, \quad (23)$$

where $\mu \equiv \hat{\mathbf{k}} \cdot \hat{\mathbf{z}}$ and

$$\Sigma_1^2 = \frac{1}{6\pi^2} \int_0^{k_s} dq [1 - j_0(q \ell_{\text{BAO}}) + 2 j_2(q \ell_{\text{BAO}})] P_{\text{nw}}(q), \quad (24)$$

$$\Sigma_2^2 = \frac{1}{2\pi^2} \int_0^{k_s} dq j_2(q \ell_{\text{BAO}}) P_{\text{nw}}(q), \quad (25)$$

with $\ell_{\text{BAO}} \simeq 110 h^{-1} \text{Mpc}$ and $k_s = 0.14 \text{Mpc}^{-1}$ (Eggemeier et al. 2025).

IR resummation is implemented by replacing $P_{\text{lin}} \rightarrow P_{\text{lin,IR}}$ throughout Sections 2.3–2.4 at three-level. At one-loop order for the power spectrum, this substitution requires an additional correction term (Ivanov & Sibiryakov 2018),

$$P_{1\text{-loop}}(k) = P_{1\text{-loop}}^{\text{SPT}}[P_{\text{lin,IR}}](k) - k^2 \Sigma_{\text{tot}}^2 e^{-k^2 \Sigma_{\text{tot}}^2} Z_1^2(\mathbf{k}) P_{\text{w}}(k). \quad (26)$$

3. The BOSS DR12 dataset

Our analysis is based on the final galaxy samples of the Baryon Oscillation Spectroscopic Survey (BOSS) Data Release 12 (DR12)¹, part of the SDSS-III programme (Dawson et al. 2013). BOSS obtained spectroscopy for luminous galaxies over a contiguous footprint of $\sim 10^4 \text{deg}^2$ split between the North and South Galactic Caps (hereafter, NGC and SGC), targeting samples designed to trace the large-scale distribution of matter and measure the baryon acoustic oscillation (BAO) feature over the redshift range $0.15 \lesssim z \lesssim 0.7$.

3.1. Redshift samples from DR12

The BOSS DR12 large-scale structure catalogues include four target selections: LOWZ, LOWZE2, LOWZE3, and CMASS (Reid et al. 2012; Beutler et al. 2017a). The LOWZ selection targets massive early-type galaxies at low redshift using colour–colour and colour–magnitude cuts designed to produce an approximately volume-limited sample. The CMASS selection targets more distant luminous red galaxies (LRGs) with cuts optimised for approximately constant stellar mass. The LOWZE2 and LOWZE3 selections are extensions of LOWZ designed to improve completeness at intermediate redshifts.

Following Reid et al. (2016), we use the combined four selections into two non-overlapping redshift bins, hereafter referred to as *low-z* and *high-z*. The combination is performed by resampling the original catalogues in redshift, retaining each galaxy in the bin corresponding to its spectroscopic redshift. The *low-z* sample covers $0.15 < z < 0.43$, with effective redshift $z_{\text{eff,low-z}} \simeq 0.38$, while the *high-z* sample spans $0.43 < z < 0.70$, with $z_{\text{eff,high-z}} \simeq 0.61$. In both cases we follow the standard BOSS data-quality cuts and veto masks. The resulting samples contain of order a few 10^5 galaxies for *low-z* and $\sim 7 \times 10^5$ for *high-z* when combining NGC and SGC.

3.2. Random catalogues and weights

To characterise the survey geometry and radial selection function we use the public BOSS DR12 random catalogues associated with the *low-z* and *high-z* samples (Reid et al. 2016). It is a catalog of unclustered objects that follow the same angular mask and redshift distribution as the data, with a density ~ 50 times higher than the corresponding galaxy catalogues. They enter all our estimators of two- and three-point statistics. All galaxies are assigned the standard BOSS total weight

$$w_{\text{tot}} = (w_{\text{rf}} + w_{\text{fc}} - 1) w_{\text{sys}}, \quad (27)$$

where w_{rf} and w_{fc} correct for redshift failures and fibre collisions, respectively, and w_{sys} accounts for large-scale angular systematics such as stellar density and seeing variations (Ross et al. 2012; Anderson et al. 2014).

3.3. MultiDark-Patchy mock catalogues

To estimate the covariance matrix of our clustering measurements and to validate the data analysis pipeline, we make use of the publicly available suite of 2048 MultiDark-Patchy mock catalogues (Klypin et al. 2016; Kitaura et al. 2016), hereafter referred to as Patchy mocks. These were generated using an ap-

¹ <https://www.sdss3.org/index.php>

¹ <https://www.skiesanduniverses.org/page/page-3/page-15/page-9/>

proximate gravity solver calibrated against full N-body simulations, and are designed to reproduce the statistical properties of the BOSS DR12 galaxy samples and the known selection effects. They are constructed for all four data chunks (NGC/SGC \times low- z /high- z), adopting the same angular mask, veto flags and radial selection function as the BOSS DR12 data described in Sec. 3.

Each mock catalogue is accompanied by a dedicated random catalogue sharing the same geometry as the data. Galaxy weights in the Patchy mocks are assigned as

$$w_{\text{tot}}^{\text{mock}} = w_{\text{veto}} w_{\text{fc}}, \quad (28)$$

comprising a veto mask term and a fibre-collision correction, but omitting the angular systematic weight w_{sys} , which is not required for synthetic catalogues.

The procedure adopted to estimate the covariance matrix from the Patchy suite, including the Hartlap correction for the finite number of realisations, is detailed in Sec. 4.1.

4. Parameter inference

We describe here the statistical framework adopted to infer cosmological and nuisance parameters in a Bayesian approach from the 2PCF and 3PCF measurements presented in Appendix B.2.1 and Appendix B.2.2. We detail the estimation of the covariance matrix (Sect. 4.1), the data-vector compression scheme adopted for the joint analysis (Sect. 4.2), the likelihood and sampling procedure (Sect. 4.3), and the goodness-of-fit diagnostics used to validate and compare the different analysis configurations (Sect. 4.5).

4.1. Covariance matrix

We estimate the covariance matrix of the data vector \mathbf{d} numerically, by applying the same 2PCF and 3PCF estimators described in App. B.1 to the full suite of $N_m = 2048$ Patchy mock catalogues. The sample covariance matrix is estimated as

$$\hat{C}_{ij} = \frac{1}{N_m - 1} \sum_{k=1}^{N_m} (d_i^k - \bar{d}_i)(d_j^k - \bar{d}_j), \quad (29)$$

where d_i^k is the value of the i -th bin in the k -th mock and \bar{d}_i is the sample mean over all realisations. The matrix has a natural block structure,

$$\hat{C} = \begin{pmatrix} \hat{C}_{\xi\xi} & \hat{C}_{\xi\zeta} \\ \hat{C}_{\zeta\xi} & \hat{C}_{\zeta\zeta} \end{pmatrix}, \quad (30)$$

where $\hat{C}_{\xi\xi}$ and $\hat{C}_{\zeta\zeta}$ quantify the covariant errors on the 2PCF and 3PCF multipoles respectively, and $\hat{C}_{\xi\zeta} = \hat{C}_{\zeta\xi}^T$ encodes their cross-covariance.

Because N_m is finite, the naive inverse \hat{C}^{-1} is a biased estimator of the true precision matrix. We apply the multiplicative correction of Hartlap et al. (2009),

$$\hat{\Psi} = \alpha_H \hat{C}^{-1}, \quad (31)$$

where

$$\alpha_H = \frac{N_m - N_d - 2}{N_m - 1} \quad (32)$$

where N_d is the size of the data vector. Furthermore, the finite number of mocks introduces an additional uncertainty in \hat{C} that propagates into the posterior widths of the inferred parameters.

Following Percival et al. (2014), we correct the marginalised parameter variances by a factor

$$\alpha_P = \frac{1 + B(N_d - N_p)}{1 + A + B(N_p + 1)}, \quad (33)$$

where N_p is the number of free parameters and

$$A = \frac{2}{(N_m - N_d - 1)(N_m - N_d - 4)}, \quad (34)$$

$$B = \frac{N_m - N_d - 2}{(N_m - N_d - 1)(N_m - N_d - 4)}. \quad (35)$$

4.2. Optimal data-vector compression

For the joint 2PCF+3PCF analysis, the combined data vector has dimension N_d large enough that the ratio N_m/N_d is insufficient to guarantee a well-conditioned covariance matrix inversion. Rather than inflating the bin sizes or discarding 3PCF configurations, we follow Philcox et al. (2021a) and compress the data vector into a low-dimensional subspace that retains, by construction, the vast majority of the cosmological information. The method proceeds by constructing a *template bank* of model vectors, analysing their covariance structure with Singular Value Decomposition (SVD), and retaining only the modes that carry the largest prior-averaged cosmological information. This yields an ordered basis in data space, where the retained modes span the directions most relevant to the inference and the discarded ones contribute negligibly to the likelihood.

The *template bank* consists of $N_{\text{bank}} = 10^4$ model evaluations drawn uniformly from the prior on the full cosmological and nuisance parameter space $\boldsymbol{\theta} = \{10^9 A_s, h, \omega_{\text{cdm}}, b_1, b_2, b_{G_2}, b_{\Gamma_3}, c_0, c_2, c_4, a_{\text{vir}}\}$. Each model vector $\mathbf{d}(\boldsymbol{\theta}^{(i)})$ is evaluated using the theory emulators described in Sec. 4.4, making the generation of the full bank computationally feasible. The template spectra are first noise-weighted and mean-subtracted,

$$X_\alpha^{(i)} = \sum_b C_{\alpha b}^{-1/2} [d_b(\boldsymbol{\theta}^{(i)}) - \bar{d}_b], \quad (36)$$

where $\bar{\mathbf{d}}$ is the mean over all templates and $C^{1/2}$ is the Cholesky decomposition of the sample covariance. Stacking the N_{bank} rotated vectors into a matrix \mathbf{X} of dimension $N_{\text{bank}} \times N_d$ and performing the Singular Value Decomposition (SVD), $\mathbf{X} = \mathbf{U} \mathbf{D} \mathbf{V}^T$, yields an ordered set of basis vectors $\{\mathbf{V}_\alpha\}$ and singular values $\{D_\alpha\}$. The basis vectors are ordered by decreasing singular value, so that the first modes span the directions in data space that carry the most prior-averaged cosmological information; modes with small D_α contribute negligibly to the likelihood and can be safely discarded.

The number of retained modes N_{SV}^* is determined by the criterion

$$N_{\text{SV}}^* = \min \left(N_{\text{SV}} \left| \frac{1}{N_{\text{bank}} \cdot N_{\text{dof}}(N_{\text{SV}})} \sum_{\alpha > N_{\text{SV}}} D_\alpha^2 \leq \Delta \tilde{\chi}_{\text{red, thr}}^2 \right. \right), \quad (37)$$

with threshold $\Delta \tilde{\chi}_{\text{red, thr}}^2 = 0.05$, where $N_{\text{dof}}(N_{\text{SV}})$ is the number of degrees of freedom corresponding to the retained subspace. This is a slight variation of the criterion explained in Philcox et al. (2021a), where we normalise by the number of degrees of freedom so that the threshold is expressed in terms of the mean *reduced* $\tilde{\chi}^2$ error incurred by the subspace projection, averaged across the prior.

The compressed covariance $\hat{C}_{\alpha\beta}^{\text{sub}}$ is estimated directly from the 2048 Patchy mocks in the projected space, and the Hartlap and Percival corrections of Eqs. (31)–(33) are applied with N_d replaced by N_{SV}^* , yielding corrections significantly closer to unity than in the uncompressed case.

4.3. Likelihood and MCMC sampling

We perform the cosmological inference in a Bayesian framework, sampling the posterior distribution of the model parameters θ . The posterior is proportional to the product of the likelihood and the prior,

$$P(\theta|\mathbf{d}) \propto \mathcal{L}(\mathbf{d}|\theta)\pi(\theta), \quad (38)$$

where $\pi(\theta)$ denotes the prior distribution. We adopt a Gaussian likelihood for the data vector \mathbf{d} ,

$$-2 \ln \mathcal{L}(\theta) = \chi^2(\theta) = (\mathbf{d} - \mathbf{m}(\theta))^T \hat{\Psi} (\mathbf{d} - \mathbf{m}(\theta)), \quad (39)$$

For the 2PCF-only analysis, $\mathbf{d} = \xi$ and $\hat{\Psi} = \hat{\Psi}_{\xi\xi}$. For the joint 2PCF+3PCF analysis, the data vector is the concatenation $\mathbf{d} = (\xi, \zeta)^T$ and the precision matrix is computed from the full joint covariance of Eq. (30), which retains the cross-covariance block $\hat{C}_{\xi\zeta}$; in this case, following the procedure described in Sec. 4.2, $\hat{\Psi}$ is obtained from the Hartlap-corrected inverse of the compressed covariance \hat{C}^{sub} .

We sample the posterior distribution using the EMCEE code (Foreman-Mackey et al. 2013), which implements an affine-invariant ensemble sampler. We employ N_{walk} walkers and terminate the chains only after each walker has accumulated at least 100 integrated autocorrelation times τ_{ac} , ensuring full convergence. Different priors are assumed for all free parameters; the complete list of parameters and prior ranges is given in Tab. 1.

4.4. Emulation of full-shape redshift-space templates

The affine-invariant ensemble sampler described above requires $O(10^5\text{--}10^6)$ evaluations of the theoretical data vector during a typical MCMC run. Direct evaluation of the configuration-space templates at every step is computationally prohibitive: while the 2PCF multipoles can be computed via one-dimensional Hankel transforms in a fraction of a second, the 3PCF requires a two-dimensional FFTLog integration over a large number of triangle configurations, making a brute-force approach unfeasible for likelihood sampling purposes. A fast emulator is therefore an essential ingredient of the analysis, and what makes a full-shape configuration-space joint analysis of the 2PCF and 3PCF practically achievable.

To this end, we construct a neural-network emulator that predicts, as a function of the cosmological and nuisance parameters θ , the full joint data vector

$$\mathbf{d} = \left\{ \xi_{s,0}(r), \xi_{s,2}(r), \xi_{s,4}(r), \zeta_{s,0,\ell}(r_{12}, r_{13}) \right\}_{\ell=0}^{\ell_{\text{max}}}, \quad (40)$$

comprising the monopole, quadrupole and hexadecapole of the 2PCF and the $(\ell_{\text{max}} + 1)$ Legendre multipoles of the isotropic 3PCF evaluated over all admissible triangle configurations (r_{12}, r_{13}) . The emulator architecture follows Euclid Collaboration: Guidi et al. (2026), to which we refer the reader for full implementation details. With respect to that work, the framework is extended to account for redshift-space

distortions and the geometric Alcock–Paczyński distortions, parametrised by the dilation parameters

$$\alpha_{\perp} = \frac{D_A(\theta) r_s^{\text{fid}}}{D_A^{\text{fid}} r_s(\theta)}, \quad \alpha_{\parallel} = \frac{H^{\text{fid}} r_s^{\text{fid}}}{H(\theta) r_s(\theta)}. \quad (41)$$

where $D_A(z)$ and $H(z)$ are the angular diameter distance, Hubble parameter at the effective redshift of each sample, r_s is the sound horizon at the drag epoch and the fiducial cosmology has been specified in Tab B.1. The training set is constructed via a Latin Hypercube Sampling (LHS) scheme over the prior volume in $(h, \omega_{\text{cdm}}, 10^9 A_s, a_{\text{vir}}) \in [(0.65, 0.75), (0.08, 0.015), (1.5, 2.6), (0, 15)]$, with 10^4 training points for the 2PCF and 4×10^3 for the 3PCF. The smaller training set for the 3PCF is justified by the smoother parameter dependence of the 3PCF templates over the explored prior volume, as verified by the accuracy diagnostics described below.

The emulator accuracy is assessed on a test set not used during training. For each test point, we evaluate the normalised residual of every element of the data vector,

$$\epsilon_{\xi}(r) \equiv \frac{\xi^{\text{emu}}(r) - \xi^{\text{exact}}(r)}{\sigma_{\xi}(r)}, \quad (42)$$

$$\epsilon_{\zeta}(r_{12}, r_{13}) \equiv \frac{\zeta^{\text{emu}}(r_{12}, r_{13}) - \zeta^{\text{exact}}(r_{12}, r_{13})}{\sigma_{\zeta}(r_{12}, r_{13})}, \quad (43)$$

which directly quantifies the fraction of the statistical error budget consumed by the emulator systematic. The normalised distributions of $|\epsilon_{\xi}|$ and $|\epsilon_{\zeta}|$ across all test points, separation bins, and multipoles are shown in Figs. 1a and 1b for the *low-z* and *high-z* samples. In all cases the distributions peak at $|\epsilon| \sim 10^{-4}\text{--}10^{-5}$, with tails not exceeding $|\epsilon| \lesssim 10^{-1}$, implying that the emulator systematic is smaller than the statistical uncertainty by at least three to four orders of magnitude at the median, and remains below 10% of σ everywhere in the explored parameter space. A mild improvement in accuracy is observed for the *high-z* sample in the 2PCF residuals, likely reflecting the different scale ranges and signal-to-noise ratios of the two samples, while the 3PCF residuals are comparable between the two bins. We therefore conclude that the emulator introduces no appreciable systematic bias into the likelihood analysis.

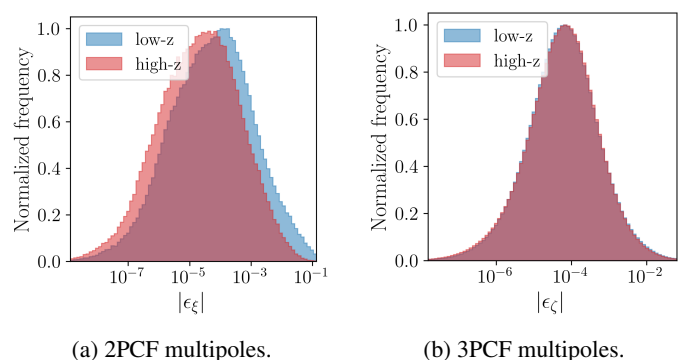


Fig. 1: Distribution of normalised emulator residuals $|\epsilon|$ for the 2PCF multipoles ($\ell = 0, 2, 4$; left) and 3PCF multipoles ($\ell = 0, 1, 2, 3, 4$; right) evaluated over a test set for the *low-z* (blue) and *high-z* (red) BOSS DR12 samples. The residuals are normalised by the diagonal of the data covariance matrix, $\sigma_{\xi}(r)$ and $\sigma_{\zeta}(r_{12}, r_{13})$, and thus quantify the emulator systematic as a fraction of the statistical error.

Table 1: Prior distributions for all free parameters. $\mathcal{U}[a, b]$ denotes a uniform prior; $\mathcal{N}(\mu, \sigma^2, a, b)$ a Gaussian truncated to $[a, b]$. Cosmological parameters are shared between redshift bins in the *combined samples* analysis; all nuisance parameters are independent per bin.

Parameter	Description	Prior
<i>Cosmological parameters</i>		
$10^9 A_s$	Scalar amplitude	$\mathcal{N}(2.145, 0.5^2, 1.0, 3.0)$
h	Hubble parameter	$\mathcal{U}[0.65, 0.75]$
ω_{cdm}	CDM density	$\mathcal{U}[0.09, 0.15]$
<i>Galaxy bias parameters</i>		
b_1	Linear bias	$\mathcal{U}[1.0, 3.0]$
b_2	Quadratic bias	$\mathcal{N}(0, 1^2, -5, 5)$
b_{G_2}	Non-local bias	$\mathcal{N}(0, 1^2, -5, 5)$
b_{Γ_3}	Third-order non-local bias	$\mathcal{N}(0.548, 1^2, -5, 5)$
<i>EFT counter-terms</i>		
c_0	Isotropic counter-term	$\mathcal{N}(0, 10^2, -10^4, 10^4)$
c_2	Quadrupole counter-term	$\mathcal{N}(0, 10^2, -10^3, 10^3)$
c_4	Hexadecapole counter-term	$\mathcal{N}(0, 10^2, -10^3, 10^3)$
<i>Velocity dispersion</i>		
a_{vir}	Virial velocity parameter	$\mathcal{N}(0, 20^2, 0, 10^3)$

4.5. Goodness of fit and Figure of Merit

To assess the goodness of fit of each analysis configuration, we compute the reduced chi-squared

$$\chi_{\text{red}}^2 = \frac{\chi^2(\hat{\theta})}{N_{\text{dof}}}, \quad (44)$$

where $\hat{\theta}$ denotes the maximum a posteriori (MAP) estimate, i.e. the point in the parameter space that maximises the posterior $p(\theta | \mathbf{d})$, and $\chi^2(\hat{\theta})$ is evaluated at that point. The number of degrees of freedom is $N_{\text{dof}} = N_{\text{SV}}^* - N_p$, where N_p is the number of free parameters. A value of χ_{red}^2 consistent with unity within the expected statistical fluctuations of order $\sqrt{2/N_{\text{dof}}}$ indicates that the model provides an adequate description of the data; systematic deviations above or below this range signal model breakdown or data over-fitting, respectively.

To quantify and compare the constraining power of the different analyses (2PCF-only and joint 2PCF+3PCF), we adopt the Figure of Merit (Albrecht et al. 2006)

$$\text{FoM}(\theta_{\text{cos}}) = \frac{1}{\sqrt{\det[S(\theta_{\text{cos}})]}}, \quad (45)$$

where $S(\theta_{\text{cos}})$ is the parameter covariance matrix of the cosmological subset $\theta_{\text{cos}} = \{10^9 A_s, h, \omega_{\text{cdm}}\}$, marginalised over all nuisance parameters and extracted from the MCMC chains. The FoM is inversely proportional to the volume of the confidence hyper-ellipsoid in cosmological parameter space: a larger FoM corresponds to tighter, less degenerate constraints. We evaluate both χ_{red}^2 and the FoM as a function of the minimum scale cut and discuss the results in Sec. 5 and Sec. 5.2.

5. Cosmological constraints

The 2PCF and 3PCF multipoles measured from the BOSS DR12 data are presented in Appendix B.2; in this section we show the cosmological inference analysis.

5.1. 2PCF

5.1.1. Analysis setup

We perform a full-shape likelihood analysis of the 2PCF multipoles measurements described in Appendix B.2.1, fitting simultaneously the monopole, quadrupole and hexadecapole ($\ell = 0, 2, 4$) using the model described in Sec. 2 and the inference framework of Sec. 4. The free parameters are the three cosmological parameters $\{10^9 A_s, h, \omega_{\text{cdm}}\}$ and the nuisance parameters $\{b_1, b_2, b_{G_2}, b_{\Gamma_3}, c_0, c_2, c_4, a_{\text{vir}}\}$, all sampled with priors as listed in Tab. 1. All remaining cosmological parameters, including the baryon density $\omega_b \equiv \Omega_b h^2$, are held fixed at the fiducial values of Tab. B.1. Following similar analyses, the priors adopted in this analysis are intentionally broad and are chosen primarily to ensure numerical stability and to restrict the sampler to physically plausible regions of parameter space. In particular, the cosmological priors on $10^9 A_s$, h , and ω_{cdm} are wide enough that the posterior constraints are data-driven, while the nuisance priors reflect theoretical expectations from perturbation theory and calibration from simulations. The baryon density ω_b is fixed to the fiducial Patchy value for internal consistency with the mock-based forward model and to avoid introducing an additional degeneracy in the 2PCF-only fit. The analysis is performed separately for the *low-z* and *high-z* redshift bins, combining the NGC and SGC sub-samples within each bin under the assumption of shared bias parameters. We also perform a joint *low-z+high-z* analysis, hereafter *combined samples*, in which the two redshift bins share the cosmological parameters but have independent sets of nuisance parameters. To assess the sensitivity of the results to the choice of minimum scale, we repeat every analysis for $r_{\text{min}} \in \{20, 30, 40, 50, 60, 70, 80\} h^{-1} \text{Mpc}$ keeping the maximum scale fixed at $r_{\text{max}} = 130 h^{-1} \text{Mpc}$.

5.1.2. Cosmological parameter constraints

We begin by assessing the validity range of the perturbative model through the diagnostics shown in Fig. 2, which presents the reduced chi-squared χ_{red}^2 and the figure of merit on the cosmological subspace, hereafter $\text{FoM}_{\text{cosmo}}$, as a function of r_{min} for the *combined samples* analysis. The data-vector sizes and the corresponding Hartlap and Percival correction factors for all scale cuts are reported in Tab. C.1 of App. C.

The upper panel shows that χ_{red}^2 , evaluated at the posterior mean, remains comfortably within the $\pm 2\sigma$ band expected for the corresponding number of degrees of freedom across the entire range of r_{min} explored. While this confirms that the model provides an acceptable fit at all scale cuts, the goodness-of-fit criterion alone does not uniquely identify the regime of validity of the perturbative model. We therefore complement this analysis with a study of the stability of the marginalised posteriors as a function of r_{min} , presented in App. C. Based on the χ^2 goodness-of-fit criterion, we adopt $r_{\text{min}} = 20 h^{-1} \text{Mpc}$ as the reference scale cut for all subsequent 2PCF analyses, in analogy with previous analyses of the same dataset (Sánchez et al. 2017a).

The lower panel shows $\text{FoM}_{\text{cosmo}}$, which quantifies the constraining power of the analysis in the $\{10^9 A_s, h, \omega_{\text{cdm}}\}$ space. It decreases steeply and monotonically as r_{min} increases, reflecting the progressive loss of information as the data vector shrinks. In particular, the $\text{FoM}_{\text{cosmo}}$ at $r_{\text{min}} = 20 h^{-1} \text{Mpc}$ is approximately three times larger than that at $r_{\text{min}} = 40 h^{-1} \text{Mpc}$, highlighting the significant gain in cosmological information retained when smaller scales are included in the analysis.

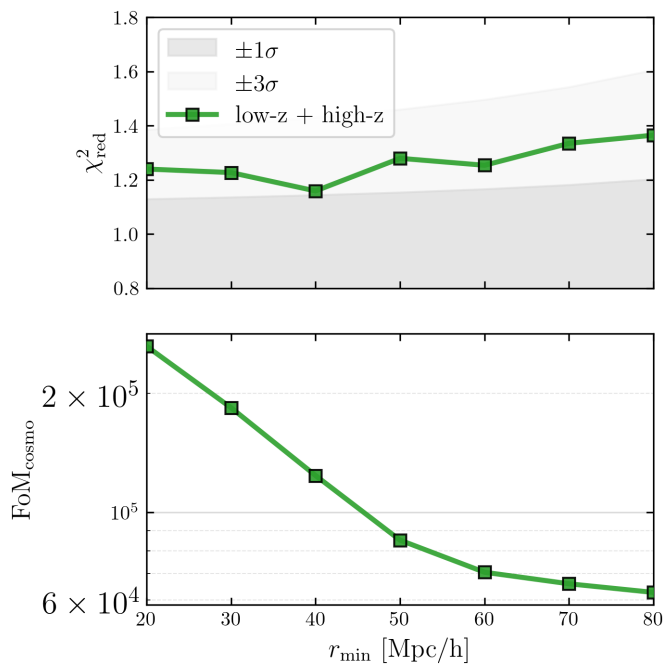


Fig. 2: Model diagnostics for the *combined samples* 2PCF analysis as a function of r_{min} , with $r_{\text{max}} = 130 h^{-1}\text{Mpc}$ fixed. *Top panel*: reduced chi-squared χ_{red}^2 at the posterior mean; dark and light grey bands mark the $\pm 1\sigma$ and $\pm 3\sigma$ expected uncertainties. *Bottom panel*: Figure of Merit on the cosmological subset $\{10^9 A_s, h, \omega_{\text{cdm}}\}$.

The marginalised posteriors of the cosmological parameters at $r_{\text{min}} = 20 h^{-1}\text{Mpc}$ are shown in Fig. 3. The diagonal panels display the one-dimensional marginal distributions of $10^9 A_s$, h and ω_{cdm} , while the off-diagonal panels show the joint 68% and 95% credible contours for the *low-z* (dashed blue), *high-z* (dashed red) and *combined samples* (filled green) analyses. The *low-z* and *high-z* bins are analysed separately and are broadly consistent within statistical uncertainties. The *high-z* posterior for ω_{cdm} is slightly broader than the *low-z* one, with the marginalised distribution extending toward the upper boundary of the prior range; this behaviour is a known feature of full-shape analyses of single BOSS DR12 redshift bins, and has been observed in analogous analyses (Ivanov et al. 2022). It reflects the limited constraining power of the high- z sample alone on the broad-band shape of the 2PCF, which encodes most of the ω_{cdm} information, rather than a systematic bias in the modelling pipeline. The *combined samples* analysis exploits the complementarity between the two redshift bins to break this degeneracy, yielding substantially tighter and well-converged constraints: $10^9 A_s = 1.736^{+0.183}_{-0.155}$, $h = 0.684 \pm 0.005$ and $\omega_{\text{cdm}} = 0.133^{+0.006}_{-0.006}$.

The Hubble parameter is the best-constrained of the three, with a $\sim 0.7\%$ precision, while $10^9 A_s$ carries the largest relative uncertainty. The 2D contours reveal a positive h - ω_{cdm} correlation, driven by the joint sensitivity of the BAO scale, and a negative A_s - ω_{cdm} correlation. The latter, discussed further in App. C, underlies the observed shift of ω_{cdm} as smaller scales are included in the analysis. As broad-band shape information is progressively added to the data vector, the degeneracy between these parameters evolves, leading to a corresponding broadening and shift of their marginalised posteriors.

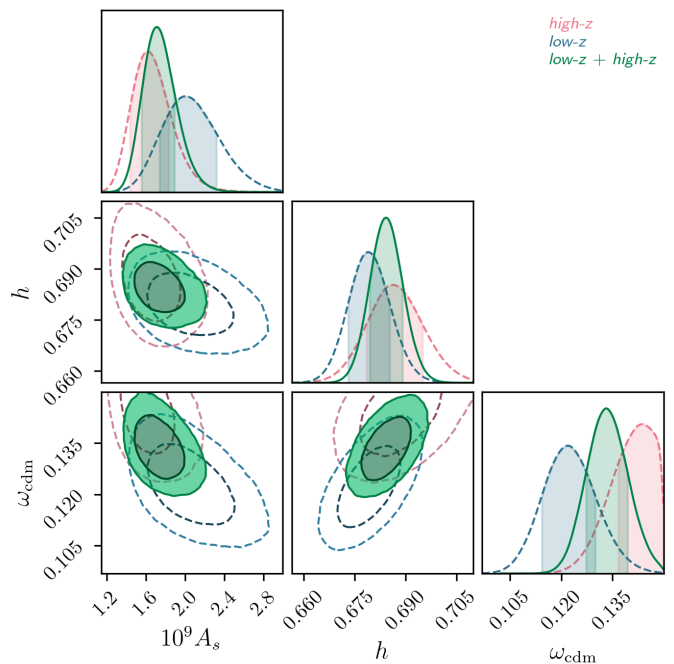


Fig. 3: Marginalised posterior distributions of the cosmological parameters $10^9 A_s$, h and ω_{cdm} from the 2PCF-only analysis at the reference scale cut $r_{\text{min}} = 20 h^{-1}\text{Mpc}$. The diagonal panels show the one-dimensional marginal distributions; the off-diagonal panels show the joint 68% and 95% credible regions. Filled green contours correspond to the *combined samples* redshift bins analysis; dashed blue and red contours show the individual *low-z* and *high-z* results, respectively.

5.2. Joint 2PCF + 3PCF

We present here the full-shape cosmological analysis combining the 2PCF and 3PCF multipoles of the BOSS DR12 *combined samples* data, whose measurements are shown in Appendix B.2. The 2PCF scale cut is fixed at $r_{\text{min}}^{2\text{PCF}} = 20 h^{-1}\text{Mpc}$ as established in Sect. 5. For the 3PCF we explore a range of $r_{\text{min}}^{3\text{PCF}} \in [40, 80] h^{-1}\text{Mpc}$ and $\eta_{\text{min}} \in \{1, 2, 3\}$, where η_{min} is a threshold on the elongation of the retained triangle configurations, defined as

$$\eta \equiv \frac{r_{13} - r_{12}}{\Delta r}, \quad (46)$$

with Δr being the separation bin size, to parametrise the proximity of a given configuration to the isosceles case. Fixing a lower limit, η_{min} , amounts to excluding isosceles, or nearly isosceles configurations (Veropalumbo et al. 2022). In particular, the case $\eta_{\text{min}} = 0$ is excluded, as it retains nearly equilateral triangle configurations that are problematic for perturbative inference at tree level; further details are given in App. B.1.

5.2.1. Scale cut selection

Figure 4 summarises the two diagnostics used to identify the reference scale cut for the joint analysis. The upper panel shows the reduced chi-squared χ_{red}^2 , evaluated at the posterior mean, as a function of $r_{\text{min}}^{3\text{PCF}}$ for the three values of η_{min} . The lower panel shows the relative FoM gain $\Delta\text{FoM}/\text{FoM}_{2\text{PCF}}$ in percent, where $\text{FoM}_{2\text{PCF}}$ represents the figure of merit of the 2PCF-only analysis at $r_{\text{min}}^{2\text{PCF}} = 20 h^{-1}\text{Mpc}$.

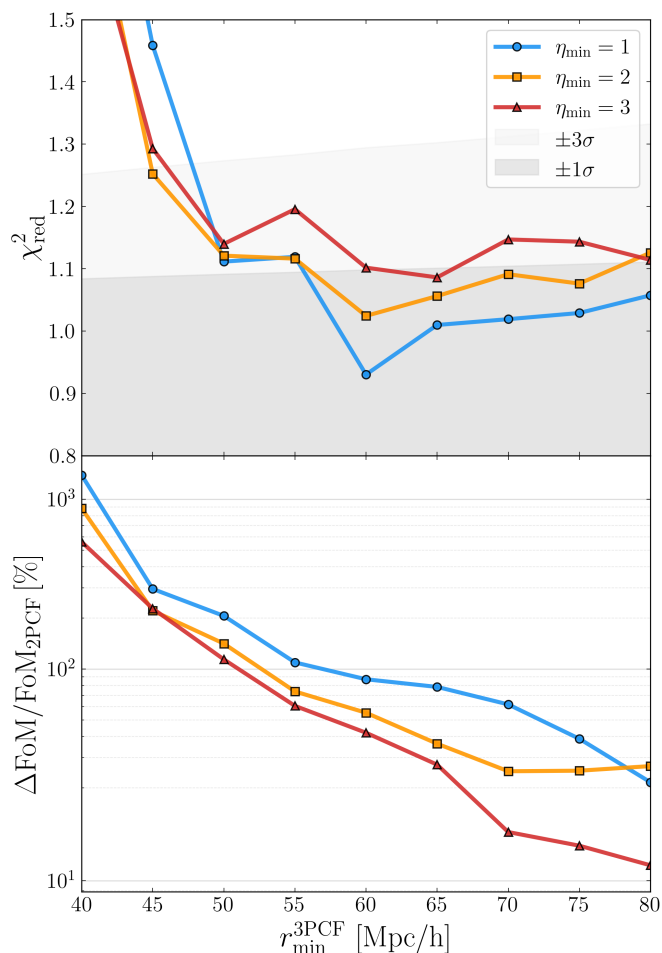


Fig. 4: Goodness-of-fit and FoM gain of the joint 2PCF+3PCF *combined samples* analysis as a function of $r_{\min}^{3\text{PCF}}$, with $r_{\min}^{2\text{PCF}} = 30 h^{-1}\text{Mpc}$ fixed. Results are shown for $\eta_{\min} = 1$ (blue), 2 (green), and 3 (orange). *Upper panel*: reduced chi-squared χ_{red}^2 evaluated at the posterior mean; grey bands mark the $\pm 1\sigma$ and $\pm 3\sigma$ expected intervals for the corresponding number of degrees of freedom, at the fixed value $\eta_{\min} = 3$. *Lower panel*: relative FoM gain $\Delta\text{FoM}/\text{FoM}_{2\text{PCF}}$ in percent on a logarithmic scale, where $\text{FoM}_{2\text{PCF}}$ is the figure of merit of the 2PCF-only analysis at $r_{\min}^{2\text{PCF}} = 20 h^{-1}\text{Mpc}$.

At $r_{\min}^{3\text{PCF}} = 40 h^{-1}\text{Mpc}$ the χ_{red}^2 exceeds the $\pm 3\sigma$ expected band for all three η_{\min} values. It decreases steeply as $r_{\min}^{3\text{PCF}}$ increases; $\eta_{\min} = 1$ and $\eta_{\min} = 2$ enter the $\pm 1\sigma$ band around $r_{\min}^{3\text{PCF}} \simeq 55\text{--}60 h^{-1}\text{Mpc}$, while $\eta_{\min} = 3$ remains slightly above the $\pm 1\sigma$ band across most of the explored range, reflecting the fact that fewer triangle configurations leave less freedom to absorb residual model imperfections. The goodness of fit is therefore driven primarily by $r_{\min}^{3\text{PCF}}$, with a secondary dependence on η_{\min} that is most visible at intermediate scale cuts. We note that the expected bands themselves are largely insensitive to η_{\min} , as the number of degrees of freedom varies negligibly across the three choices.

The lower panel reveals a complementary picture. The FoM gain decreases monotonically as $r_{\min}^{3\text{PCF}}$ increases, and a clear hierarchy among the three elongation cuts is present across the entire range: $\eta_{\min} = 1 > \eta_{\min} = 2 > \eta_{\min} = 3$. This ordering directly reflects the information content of the different triangle subsets: smaller η_{\min} admits a larger number of configurations, in

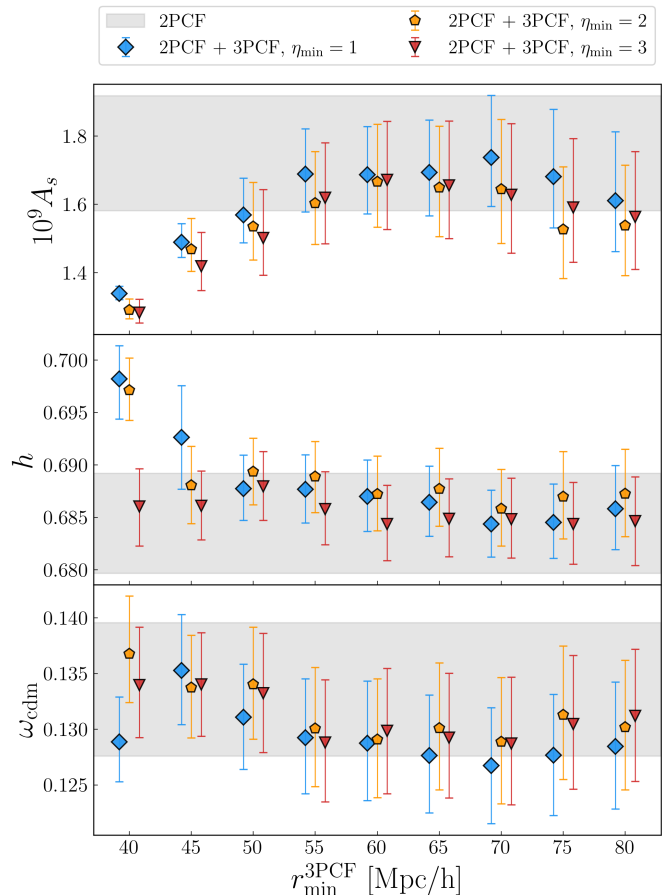


Fig. 5: Marginalised posterior means and 68% credible intervals for $10^9 A_s$ (top), h (middle) and ω_{cdm} (bottom) from the joint 2PCF+3PCF *combined samples* analysis as a function of $r_{\min}^{3\text{PCF}}$, for $\eta_{\min} = 1$ (blue diamonds), 2 (green pentagons) and 3 (orange triangles). The grey dashed line and shaded band show the posterior mean and 1σ interval of the 2PCF-only reference analysis at $r_{\min}^{2\text{PCF}} = 20 h^{-1}\text{Mpc}$. The dotted line marks the Patchy fiducial value.

particular squeezed and nearly-degenerate triangles, which carry additional cosmological signal. At $r_{\min}^{3\text{PCF}} = 60 h^{-1}\text{Mpc}$ the FoM gains are approximately 90%, 55% and 40% for $\eta_{\min} = 1, 2$ and 3 respectively; at $r_{\min}^{3\text{PCF}} = 70 h^{-1}\text{Mpc}$ they reduce to approximately 60%, 25% and 15%.

To report our results, we adopt $r_{\min}^{3\text{PCF}} = 60 h^{-1}\text{Mpc}$ with $\eta_{\min} = 1$ as a reference configuration for the joint analysis: this is the a conservative choice on the smallest scale cut at which the model is statistically acceptable, and it retains the largest FoM gain consistent with perturbative validity. The validity of this choice is further supported by the stability of the marginalised posteriors as a function of $r_{\min}^{3\text{PCF}}$, discussed in Sect. 5.2.2. The configurations $r_{\min}^{3\text{PCF}} = 60 h^{-1}\text{Mpc}$ with $\eta_{\min} = 2$ and 3, and $r_{\min}^{3\text{PCF}} = 70 h^{-1}\text{Mpc}$ with $\eta_{\min} = 3$, are used as robustness checks.

5.2.2. Cosmological constraints

Figure 5 shows the marginalised posterior means and 68% and 99.7% credible intervals of the cosmological subset $10^9 A_s$, h ,

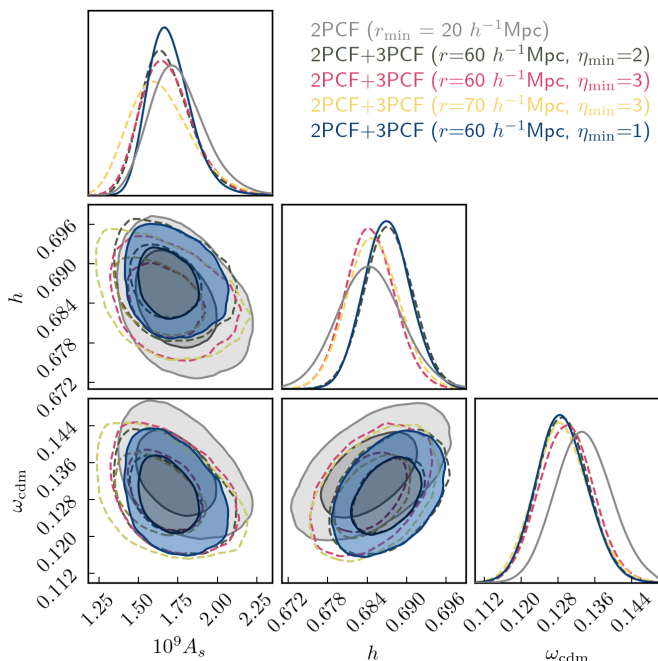


Fig. 6: Marginalised posterior distributions of $10^9 A_s$, h and ω_{cdm} for the joint 2PCF+3PCF combined samples analysis. Grey: 2PCF-only result at $r_{\text{min}}^{\text{2PCF}} = 20 h^{-1}\text{Mpc}$. Filled dark green: reference joint analysis ($r_{\text{min}}^{\text{3PCF}} = 60 h^{-1}\text{Mpc}$, $\eta_{\text{min}} = 3$). Dashed pink: $r_{\text{min}}^{\text{3PCF}} = 70 h^{-1}\text{Mpc}$, $\eta_{\text{min}} = 2$. Dashed blue: $r_{\text{min}}^{\text{3PCF}} = 70 h^{-1}\text{Mpc}$, $\eta_{\text{min}} = 3$. Different contours enclose the 68% and 95% credible regions.

and ω_{cdm} as a function of $r_{\text{min}}^{\text{3PCF}}$, for three choices of the elongation cut $\eta_{\text{min}} \in \{1, 2, 3\}$; the grey band marks the 2PCF-only reference constraint. At small $r_{\text{min}}^{\text{3PCF}}$ values, the three parameters exhibit a coherent drift with respect to the 2PCF-only baseline: $10^9 A_s$ decreases, h increases, and ω_{cdm} shifts more mildly in the same direction. This pattern is consistent with the elevated χ_{red}^2 at those scales (Fig. 4) and indicates that the joint model is operating close to the edge of its validated perturbative range. As $r_{\text{min}}^{\text{3PCF}}$ increases, the posterior means converge progressively toward the 2PCF-only band, and from $r_{\text{min}}^{\text{3PCF}} \simeq 60 h^{-1}\text{Mpc}$ onward all three parameters are stable and mutually consistent across all elongation cuts.

Figure 6 compares the full marginalised posterior distributions of $\{10^9 A_s, h, \omega_{\text{cdm}}\}$ for the 2PCF-only baseline (grey) and for four joint configurations: $r_{\text{min}}^{\text{3PCF}} = 60 h^{-1}\text{Mpc}$ with $\eta_{\text{min}} = 1, 2$, and 3 (dark blue, dashed pink, and dashed magenta, respectively), together with the additional robustness run at $r_{\text{min}}^{\text{3PCF}} = 70 h^{-1}\text{Mpc}$, $\eta_{\text{min}} = 3$ (dashed yellow). All considered joint configurations yield mutually consistent posteriors, confirming the robustness of the results against the specific choice of $r_{\text{min}}^{\text{3PCF}}$ and η_{min} within the validated range.

The inclusion of the 3PCF improves the constraints on all three cosmological parameters, with a gain that depends on both the scale cut and the elongation threshold. At the reference configuration ($r_{\text{min}}^{\text{3PCF}} = 60 h^{-1}\text{Mpc}$, $\eta_{\text{min}} = 1$), the joint analysis yields $10^9 A_s = 1.687^{+0.141}_{-0.154}$, $h = 0.687 \pm 0.0035$, and $\omega_{\text{cdm}} = 0.1288^{+0.0056}_{-0.0052}$. The 1σ uncertainty on h shrinks from ± 0.0048 in the 2PCF-only baseline to ± 0.0035 , a reduction of 29%, making it the parameter that benefits most from the addition of the 3PCF. The constraint on ω_{cdm} improves by 10%,

while the $10^9 A_s$ posterior narrows by 24%, though its central value shifts by less than 0.3σ with respect to the 2PCF-only result. This hierarchy confirms that, at the adopted scale cuts, the 3PCF contributes primarily through the geometric and redshift-space distortion sector of parameter space, with an appreciable but secondary effect on the clustering amplitude.

The gain on h is robust across all configurations explored: even the most conservative choice ($r_{\text{min}}^{\text{3PCF}} = 70 h^{-1}\text{Mpc}$, $\eta_{\text{min}} = 3$) yields a 20% improvement on $\sigma(h)$. The improvement on $10^9 A_s$ is instead more sensitive to the scale cut: it reaches 24% at $r_{\text{min}}^{\text{3PCF}} = 60 h^{-1}\text{Mpc}$, but becomes negligible or even slightly negative at larger $r_{\text{min}}^{\text{3PCF}}$, indicating that the amplitude information is concentrated in the smaller-scale triangle configurations. The central values of all three parameters are stable across configurations, with shifts well within the respective 1σ intervals, confirming the robustness of the cosmological inference within the validated range.

6. Discussion and conclusion

We have presented the first full-shape redshift-space joint analysis combining the 2PCF and 3PCF on real data, applied to the BOSS DR12 combined sample across two redshift bins. This analysis constitutes a milestone on several fronts:

- for the first time, a full-shape cosmological inference jointly combining the 2PCF and 3PCF has been performed on observational data, accounting for both redshift-space distortions and Alcock–Paczynski effects developing a dedicated emulator. This extends to the full redshift-space case the joint analysis previously validated in real space by [Euclid Collaboration: Guidi et al. \(2026\)](#);
- the redshift-space 3PCF is modelled here for the first time within the VDG framework, extending to configuration space the approach developed for the bispectrum in [Eggemeier et al. \(2025\)](#);
- optimal data-vector compression ([Philcox et al. 2021a](#)) is applied for the first time to a joint 2PCF and 3PCF likelihood analysis, enabling a stable inversion of the joint covariance matrix without discarding any cosmologically informative 3PCF configurations.

6.1. Main results

First, we have performed a full-shape 2PCF-only analysis of the combined sample. The reference scale cut $r_{\text{min}} = 20 h^{-1}\text{Mpc}$ was selected through a goodness-of-fit criterion: the reduced χ_{red}^2 remains statistically acceptable down to this scale, indicating that the perturbative model provides a good description of the data, while the posteriors have fully stabilised. The resulting combined-sample constraints are $10^9 A_s = 1.736^{+0.183}_{-0.155}$, $h = 0.684 \pm 0.005$ and $\omega_{\text{cdm}} = 0.133^{+0.006}_{-0.006}$, with the two redshift bins mutually consistent within 1σ for all three parameters. The reduced Hubble parameter h is the best-constrained of the three, with a $\sim 0.7\%$ precision already at the two-point level, driven by the sensitivity of the 2PCF to the BAO scale.

For the joint 2PCF and 3PCF analysis, with the 2PCF scale cut fixed at $r_{\text{min}}^{\text{2PCF}} = 20 h^{-1}\text{Mpc}$, the reference 3PCF scale cut was identified by inspecting the goodness-of-fit, considered here as a performance metric of the modelling as well as the figure of merit, as detailed in Sect. 5.2.1. The diagnostic consistently points to $r_{\text{min}}^{\text{3PCF}} = 60 h^{-1}\text{Mpc}$ with $\eta_{\text{min}} = 1$ as the reference configuration, which represent our conservative choice on the

minimum scale for which the model is statistically acceptable, and retains a FoM gain of $\sim 90\%$ over the 2PCF-only baseline. The inclusion of the 3PCF improves the constraints on all three cosmological parameters at aforementioned reference configuration yielding $10^9 A_s = 1.687^{+0.141}_{-0.154}$, $h = 0.687 \pm 0.0035$, and $\omega_{\text{cdm}} = 0.1288^{+0.0056}_{-0.0052}$. The largest gain is on h , whose uncertainty shrinks by 29%, followed by A_s (24%) and ω_{cdm} (10%). This hierarchy reflects the fact that, at the adopted scale cuts, the 3PCF primarily breaks degeneracies through the angular scale of the BAO feature, constraining h , and through the matter–radiation equality scale encoded in the shape of the correlation function, constraining ω_{cdm} , while the contribution along the A_s direction is limited because the b_1 – A_s degeneracy is only partially lifted by the triangle configurations included in the analysis. The gain on h and ω_{cdm} is stable across all triangle configurations at $r_{\text{min}}^{\text{3PCF}} = 60 h^{-1} \text{Mpc}$, while the improvement on A_s is slightly more sensitive to η_{min} . Full details are given in Sect. 5.2.2.

6.2. Comparison with the literature

The results above are fully consistent with the broader picture emerging from full-shape analyses of BOSS DR12 in Fourier space. A joint analysis of the power spectrum and bispectrum monopole of the same dataset was first performed by Gil-Marín et al. (2015, 2017) within a perturbative RSD model, finding a significant improvement on $f\sigma_8$ from the inclusion of the bispectrum. The present work extends this analysis to configuration space within a more complete theoretical framework accounting for both RSD and the AP effect, inferring the primary cosmological parameters directly in a full-shape analysis for the first time.

The interpretation requires care given the different parameter spaces. Fourier-space EFTofLSS analyses typically vary all five primary ΛCDM parameters with priors on ω_b and n_s (Ivanov et al. 2022; D’Amico et al. 2020; Philcox & Ivanov 2022; D’Amico et al. 2024), whereas in the present analysis both are held fixed to the reference Planck cosmology. Fixing n_s removes the degeneracy with the broad-band shape, tightening the posteriors on ω_{cdm} and A_s relative to the free- n_s case. More importantly for the comparison of h constraints, fixing ω_b eliminates the degeneracy between the baryon density and the sound horizon scale, which in analyses that vary ω_b , even with a BBN or Planck prior, propagates directly into the h posterior through the BAO measurement. This is the primary reason why our $\sigma(h)$ is tighter than that reported by Fourier-space analyses varying the full parameter set, and should be borne in mind when interpreting the comparison below.

Our constraint on the Hubble parameter, $h = 0.681 \pm 0.005$ from the 2PCF-only analysis and $h = 0.687 \pm 0.003$ from the joint 2PCF+3PCF analysis, is in good agreement with the range $h \simeq 0.68$ – 0.70 consistently reported by Fourier-space full-shape analyses of the same dataset. The precision achieved is competitive with Fourier-space analyses that include the bispectrum: Philcox & Ivanov (2022) report $\sigma(h) \simeq 0.009$ with a Planck prior on n_s , while D’Amico et al. (2024) obtain $\sigma(h) = 0.011$ from the joint one-loop power spectrum and bispectrum. The inferred cold dark matter density, $\omega_{\text{cdm}} = 0.127 \pm 0.007$ from the 2PCF-only analysis and $\omega_{\text{cdm}} = 0.1288 \pm 0.0054$ from the joint analysis, is in good agreement with Fourier-space analyses employing a Planck prior on n_s : Philcox & Ivanov (2022) find $\omega_{\text{cdm}} = 0.1227 \pm 0.0056$ and D’Amico et al. (2024) obtain $\Omega_m = 0.311 \pm 0.010$ (corresponding to $\omega_{\text{cdm}} \approx 0.122$). Without a Planck prior on n_s , Fourier-space analyses find systemati-

cally higher values $\omega_{\text{cdm}} \simeq 0.137$ – 0.141 with larger uncertainties (Philcox & Ivanov 2022), as expected from the ω_{cdm} – n_s degeneracy in the broad-band shape. Our constraint on A_s is broadly consistent with the amplitude constraints from the same dataset (Philcox & Ivanov 2022; D’Amico et al. 2024), with residual uncertainty reflecting the b_1 – A_s degeneracy only partially broken by the multipole structure of the two- and three-point statistics.

The gain achieved by combining 2PCF and 3PCF is quantitatively consistent with Sugiyama et al. (2021), who report a $\sim 30\%$ reduction in $\sigma(H(z))$ from the inclusion of the anisotropic 3PCF over the 2PCF pre-reconstruction baseline, decreasing to $\sim 20\%$ on top of a reconstructed field. Our analysis recovers a 29% reduction in $\sigma(h)$, 24% in $\sigma(A_s)$, and 10% in $\sigma(\omega_{\text{cdm}})$ without any density-field reconstruction, in close agreement with these predictions. A direct quantitative comparison with the 15–20% gain reported in Alam et al. (2017) requires care, as that result applies to $H(z)r_s$ rather than to absolute cosmological parameters; the comparison is therefore best understood as analogical. Beyond this analogy, the two strategies differ fundamentally in scope: post-reconstruction BAO sharpens the acoustic peak but contributes no additional information on A_s or ω_{cdm} beyond what the full-shape 2PCF already provides, whereas the 3PCF simultaneously contributes acoustic scale and broad-band information. The partial overlap between the two strategies, reflected in the reduction from $\sim 30\%$ to $\sim 20\%$ in Sugiyama et al. (2021) when the 3PCF is added on top of a reconstructed 2PCF, suggests that combining 3PCF full-shape measurements with post-reconstruction BAO could yield further improvements beyond either strategy alone.

6.3. Future perspectives

This work opens several directions for future investigation. A natural extension is the inclusion of additional cosmological parameters in the inference, both within ΛCDM and beyond, possibly including primordial non-Gaussianity, for which the three-point statistics are a primary observable carrying sensitivity to scale-dependent bias on large scales, and massive neutrinos, whose suppression of small-scale power leaves correlated imprints on both the 2PCF and the 3PCF. The relevance of higher-order statistics for beyond- ΛCDM in a similar inference analysis has been further demonstrated by Lu et al. (2025), who find a preference for evolving dark energy in a joint one-loop power spectrum and bispectrum analysis of the same dataset explored in this work. This motivates extending the present framework to beyond- ΛCDM cosmologies, where the joint 2PCF and 3PCF analysis provides a natural configuration-space counterpart. A first step in this direction, exploring neutrino imprints in the 3PCF has been shown in Labate et al. (2026). Moreover, the inclusion of the anisotropic 3PCF with respect to the line-of-sight would encode additional information on RSD beyond the monopole retained here, potentially tightening cosmological constraints. On the modelling side, extending the one-loop prediction for the 3PCF from the dark matter case, as shown in Guidi et al. (2023), to the full galaxy bias expansion would allow smaller scale cuts to be adopted, increasing the information content of the analysis and potentially improving the constraining power. On the other hand, the inference approach developed in this work is directly applicable to next-generation spectroscopic surveys such as DESI (Adame et al. 2025b) and Euclid (Euclid Collaboration: Mellier et al. 2025), where the larger survey volume and higher galaxy number density will substantially amplify the constraining power of the joint analysis.

Acknowledgements. We thank Azadeh Moradinezhad Dizgah, Farshad Kamalinejad, Zachary Slepian, Krister Nagainis, and Enzo Branchini for useful discussions. MG and MM acknowledge support from the MIUR PRIN 2022 grant "Optimizing the extraction of cosmological information from Large Scale Structure analysis in view of the next large spectroscopic surveys" (grant 2022N2ZRS001). Computational resources were provided by INFN Sezione di Genova, Bologna Physics and Astrophysics Department and Leonardo supercomputing facilities at CINECA through the INAF grants INA24C3B12 and INA24C7B06. We thank the INFN IT personnel in Genova for their continuous support. This project has received funding from the European Union Horizon Europe Research and Innovation Action under grant agreement no. 101183153-WST. Views and opinions expressed are however those of the author(s) only and do not necessarily reflect those of the European Union or the European Research Executive Agency (REA). Neither the European Union nor the REA can be held responsible for them.

References

- Adame, A. G., Aguilar, J., Ahlen, S., et al. 2025a, *JCAP*, 02, 021
- Adame, A. G., Aguilar, J., Ahlen, S., et al. 2025b, *J. Cosmology Astropart. Phys.*, 2025, 021
- Alam, S., Ata, M., Bailey, S., et al. 2017, *MNRAS*, 470, 2617
- Albrecht, A., Bernstein, G., Cahn, R., et al. 2006, arXiv:astro-ph/0609591
- Anderson, L., Aubourg, É., Bailey, S., et al. 2014, *MNRAS*, 441, 24
- Baldauf, T., Mirbabayi, M., Simonović, M., & Zaldarriaga, M. 2015, *Phys. Rev. D*, 92, 043514
- Baldauf, T., Seljak, U., Desjacques, V., & McDonald, P. 2012, *Phys. Rev. D*, 86, 083540
- Baumann, D., Nicolis, A., Senatore, L., & Zaldarriaga, M. 2012, *JCAP*, 07, 051
- Bernardeau, F., Colombi, S., Gaztañaga, E., & Scoccimarro, R. 2002, *Phys. Rep.*, 367, 1
- Beutler, F., Saito, S., Brownstein, J. R., et al. 2014, *MNRAS*, 444, 3501
- Beutler, F., Seo, H.-J., Ross, A. J., et al. 2017a, *MNRAS*, 464, 3409
- Beutler, F., Seo, H.-J., Saito, S., et al. 2017b, *MNRAS*, 466, 2242
- Blas, D., Garny, M., Ivanov, M. M., & Sibiriyakov, S. 2016, *JCAP*, 07, 052
- Cabass, G., Ivanov, M. M., Philcox, O. H. E., Simonović, M., & Zaldarriaga, M. 2022, *Phys. Rev. Lett.*, 129, 021301
- Carlson, J., Reid, B., & White, M. 2013, *MNRAS*, 429, 1674
- Carrasco, J. J. M., Hertzberg, M. P., & Senatore, L. 2012, *Journal of High Energy Physics*, 9, 82
- Chan, K. C., Scoccimarro, R., & Sheth, R. K. 2012, *Phys. Rev. D*, 85, 083509
- Crocce, M., & Scoccimarro, R. 2008, *Phys. Rev. D*, 77, 023533
- D'Amico, G., Donath, Y., Lewandowski, M., Senatore, L., & Zhang, P. 2024, *JCAP*, 05, 059
- D'Amico, G., Gleyzes, J., Kokron, N., et al. 2020, *JCAP*, 05, 005
- D'Amico, G., Lewandowski, M., Senatore, L., & Zhang, P. 2025, *Phys. Rev. D*, 111, 063514
- Dawson, K. S., Schlegel, D. J., Ahn, C. P., et al. 2013, *AJ*, 145, 10
- DESI Collaboration, Aghamousa, A., Aguilar, J., et al. 2016, arXiv:1611.00036
- Desjacques, V., Crocce, M., Scoccimarro, R., & Sheth, R. K. 2010, *Phys. Rev. D*, 82, 103529
- Eggemeier, A., Lee, N., Scoccimarro, R., et al. 2025, *Phys. Rev. D*, 112, 063532
- Eggemeier, A., Scoccimarro, R., & Smith, R. E. 2019, *Phys. Rev. D*, 99, 123514
- Eisenstein, D. J., Seo, H.-J., & White, M. 2007, *ApJ*, 664, 660
- Eisenstein, D. J., Zehavi, I., Hogg, D. W., et al. 2005, *ApJ*, 633, 560
- Euclid Collaboration: Guidi, M., Veropalumbo, A., Pugno, A., et al. 2026, *A&A*, 707, A228
- Euclid Collaboration: Mellier, Y., Abdurro'uf, Acevedo Barroso, J., et al. 2025, *A&A*, 697, A1
- Euclid Collaboration: Veropalumbo, A., Moresco, M., Marulli, F., et al. 2026, arXiv e-prints, arXiv:2605.03012
- Fang, X., Eifler, T., & Krause, E. 2020, *MNRAS*, 497, 2699
- Farina, A., Veropalumbo, A., Branchini, E., & Guidi, M. 2026, *J. Cosmology Astropart. Phys.*, 2026, 028
- Foreman-Mackey, D., Hogg, D. W., Lang, D., & Goodman, J. 2013, *PASP*, 125, 306
- Forero-Sánchez, D., Novell Masot, S., Gil-Marín, H., et al. 2026, arXiv e-prints, arXiv:2606.23936
- Fry, J. N. 1984, *ApJ*, 279, 499
- Fry, J. N. 1994, *Physical Review Letters*, 73, 215
- Fry, J. N. & Gaztañaga, E. 1993, *ApJ*, 413, 447
- Gil-Marín, H., Noreña, J., Verde, L., et al. 2015, *MNRAS*, 451, 539
- Gil-Marín, H., Percival, W. J., Verde, L., et al. 2017, *MNRAS*, 465, 1757
- Guidi, M., Veropalumbo, A., Branchini, E., Eggemeier, A., & Carbone, C. 2023, *JCAP*, 08, 066
- Guzzo, L., Pierleoni, M., Meneux, B., et al. 2008, *Nature*, 451, 541
- Hartlap, J., Schrabback, T., Simon, P., & Schneider, P. 2009, *A&A*, 504, 689
- Hivon, E., Bouchet, F. R., Colombi, S., & Juszkiewicz, R. 1995, *A&A*, 298, 643
- Ivanov, M. M., Philcox, O. H. E., Nishimichi, T., et al. 2022, *Phys. Rev. D*, 105, 063512
- Ivanov, M. M. & Sibiriyakov, S. 2018, *JCAP*, 07, 053
- Ivanov, M. M., Simonović, M., & Zaldarriaga, M. 2020, *JCAP*, 05, 042
- Kaiser, N. 1987, *MNRAS*, 227, 1
- Kamalinejad, F., Slepian, Z., Krolewski, A., et al. 2026, arXiv e-prints, arXiv:2602.16134
- Kitaura, F.-S., Rodríguez-Torres, S., Chuang, C.-H., et al. 2016, *MNRAS*, 456, 4156
- Klypin, A., Yepes, G., Gottlöber, S., Prada, F., & Heß, S. 2016, *MNRAS*, 457, 4340
- Kuruvilla, J. & Porciani, C. 2020, *JCAP*, 07, 043
- Labate, A., Guidi, M., Moresco, M., & Veropalumbo, A. 2026, *A&A*, 708, A210
- Landy, S. D. & Szalay, A. S. 1993, *ApJ*, 412, 64
- Lu, Z., Simon, T., & Zhang, P. 2025, arXiv e-prints, arXiv:2503.04602
- Marulli, F., Veropalumbo, A., & Moresco, M. 2016, *Astronomy and Computing*, 14, 35
- Matsubara, T. 2008a, *Phys. Rev. D*, 78, 109901
- Matsubara, T. 2008b, *Phys. Rev. D*, 77, 063530
- Moradinezhad Dizgah, A., Biagetti, M., Sefusatti, E., Desjacques, V., & Noreña, J. 2021, *JCAP*, 05, 015
- Moresco, M., Marulli, F., Baldi, M., Moscardini, L., & Cimatti, A. 2014, *MNRAS*, 443, 2874
- Moresco, M., Marulli, F., Moscardini, L., et al. 2017, *A&A*, 604, A133
- Moresco, M., Veropalumbo, A., Marulli, F., Moscardini, L., & Cimatti, A. 2021, *ApJ*, 919, 144
- Novell-Masot, S., Gil-Marín, H., Verde, L., et al. 2025, *J. Cosmology Astropart. Phys.*, 2025, 005
- Novell-Masot, S., Gil-Marín, H., Verde, L., et al. 2026, arXiv e-prints, arXiv:2603.19356
- Peacock, J. A., Cole, S., Norberg, P., et al. 2001, *Nature*, 410, 169
- Percival, W. J., Ross, A. J., Sánchez, A. G., et al. 2014, *MNRAS*, 439, 2531
- Philcox, O. H. E. & Ivanov, M. M. 2022, *Phys. Rev. D*, 105, 043517
- Philcox, O. H. E., Ivanov, M. M., Zaldarriaga, M., Simonović, M., & Schmittfull, M. 2021a, *Phys. Rev. D*, 103, 043508
- Philcox, O. H. E., Slepian, Z., Hou, J., et al. 2021b, arXiv e-prints, arXiv:2105.08722
- Pugno, A., Eggemeier, A., Porciani, C., & Kuruvilla, J. 2025, *JCAP*, 01, 075
- Reid, B., Ho, S., Padmanabhan, N., et al. 2016, *MNRAS*, 455, 1553
- Reid, B. A., Samushia, L., White, M., et al. 2012, *MNRAS*, 426, 2719
- Ross, A. J., Percival, W. J., Sánchez, A. G., et al. 2012, *MNRAS*, 424, 564
- Ross, N. P., da Ángela, J., Shanks, T., et al. 2007, *MNRAS*, 381, 573
- Sánchez, A. G., Grieb, J. N., Salazar-Albornoz, S., et al. 2017a, *MNRAS*, 464, 1493
- Sánchez, A. G., Kazin, E. A., Beutler, F., et al. 2013, *MNRAS*, 433, 1202
- Sánchez, A. G., Scoccimarro, R., Crocce, M., et al. 2017b, *MNRAS*, 464, 1640
- Scoccimarro, R. 1997, *ApJ*, 487, 1
- Scoccimarro, R. 2000, *ApJ*, 542, 1
- Scoccimarro, R., Couchman, H. M. P., & Frieman, J. A. 1999, *ApJ*, 517, 531
- Scoccimarro, R., Sefusatti, E., & Zaldarriaga, M. 2004, *Phys. Rev. D*, 69, 103513
- Sefusatti, E. & Komatsu, E. 2007, *Phys. Rev. D*, 76, 083004
- Senatore, L. & Zaldarriaga, M. 2015, *JCAP*, 02, 013
- Seo, H.-J. & Eisenstein, D. J. 2003, *ApJ*, 598, 720
- Slepian, Z. & Eisenstein, D. J. 2015, *MNRAS*, 454, 4142
- Slepian, Z. & Eisenstein, D. J. 2018, *MNRAS*, 478, 1468
- Slepian, Z., Eisenstein, D. J., Brownstein, J. R., et al. 2017, *MNRAS*, 469, 1738
- Smith, R. E., Scoccimarro, R., & Sheth, R. K. 2007, *Phys. Rev. D*, 75, 063512
- Sugiyama, N. S., Saito, S., Beutler, F., & Seo, H.-J. 2019, *MNRAS*, 484, 364
- Sugiyama, N. S., Saito, S., Beutler, F., & Seo, H.-J. 2021, *MNRAS*, 501, 2862
- Szapudi, I. & Szalay, A. S. 1998, *ApJ*, 494, L41
- Umeh, O. 2021, *JCAP*, 05, 035
- Verde, L., Wang, L., Heavens, A. F., & Kamionkowski, M. 2000, *MNRAS*, 313, 141
- Veropalumbo, A., Binetti, A., Branchini, E., et al. 2022, *JCAP*, 09, 033
- Veropalumbo, A., Sáez Casares, I., Branchini, E., et al. 2021, *MNRAS*, 507, 1184
- Wang, L., Reid, B., & White, M. 2014, *MNRAS*, 437, 588

Appendix A: Perturbation Theory

A.1. Definitions and conventions

We define the loop integration measure as

$$\int_{\mathbf{q}} \equiv \int \frac{d^3q}{(2\pi)^3}, \quad (\text{A.1})$$

and adopt the Fourier convention

$$\delta(\mathbf{k}) \equiv (2\pi)^3 \int_{\mathbf{x}} \delta(\mathbf{x}) e^{i\mathbf{k}\cdot\mathbf{x}}, \quad (\text{A.2})$$

$$\delta(\mathbf{x}) \equiv \int_{\mathbf{k}} \delta(\mathbf{k}) e^{-i\mathbf{k}\cdot\mathbf{x}}. \quad (\text{A.3})$$

Under statistical homogeneity and isotropy in the plane-parallel approximation, the redshift-space power spectrum is defined by

$$\langle \delta_s(\mathbf{k}_1) \delta_s(\mathbf{k}_2) \rangle \equiv (2\pi)^3 \delta_{\text{D}}(\mathbf{k}_1 + \mathbf{k}_2) P_s(\mathbf{k}_1), \quad (\text{A.4})$$

and decomposed into Legendre multipoles as

$$P_{s,\ell}(k) \equiv \frac{2\ell+1}{2} \int_{-1}^1 d\mu P_s(k, \mu) \mathcal{L}_\ell(\mu), \quad \mu \equiv \hat{\mathbf{k}} \cdot \hat{\mathbf{n}}, \quad (\text{A.5})$$

with $\ell = 0, 2, 4$. The redshift-space bispectrum is defined by

$$\langle \delta_s(\mathbf{k}_1) \delta_s(\mathbf{k}_2) \delta_s(\mathbf{k}_3) \rangle \equiv (2\pi)^3 \delta_{\text{D}}(\mathbf{k}_1 + \mathbf{k}_2 + \mathbf{k}_3) B_s(\mathbf{k}_1, \mathbf{k}_2), \quad (\text{A.6})$$

and the redshift-space 3PCF by

$$\zeta_s(\mathbf{r}_{12}, \mathbf{r}_{13}) \equiv \langle \delta_s(\mathbf{r}_1) \delta_s(\mathbf{r}_2) \delta_s(\mathbf{r}_3) \rangle, \quad (\text{A.7})$$

where $\mathbf{r}_{ij} \equiv \mathbf{r}_i - \mathbf{r}_j$. Both statistics depend on two distinct angular structures: the orientation of the triangle with respect to the line of sight, and the internal shape of the triangle.

A.2. Angular decomposition of bispectrum and 3PCF

In this work we restrict to the *monopole* of the 3PCF and bispectrum over the line-of-sight (LOS) orientation (Scoccimarro 1997; Slepian & Eisenstein 2015; Sugiyama et al. 2019), i.e. we average over all orientations of the triangle with respect to the LOS, retaining only the dependence on the internal triangle shape. The residual dependence on the internal angle $\mu_{12} \equiv \hat{\mathbf{k}}_1 \cdot \hat{\mathbf{k}}_2$ (or $\mu_{12,13} \equiv \hat{\mathbf{r}}_{12} \cdot \hat{\mathbf{r}}_{13}$ in configuration space) is then expanded in Legendre polynomials up to a given ℓ_{max} .

Bispectrum. Following Scoccimarro (1997), the bispectrum is first expanded in spherical harmonics with respect to the orientation of \mathbf{k}_1 relative to the LOS $\hat{\mathbf{n}}$,

$$B_s(\mathbf{k}_1, \mathbf{k}_2) = \sum_{L,M} B_{s,L}^M(k_1, k_2, \mu_{12}) Y_L^M(\omega_{k_1}, \theta_{k_1}), \quad (\text{A.8})$$

where ω_{k_1} and θ_{k_1} are the polar and azimuthal angles of \mathbf{k}_1 with respect to $\hat{\mathbf{n}}$, and we have assumed invariance under rotations in the plane orthogonal to $\hat{\mathbf{n}}$. The multipole coefficients are

$$B_{s,L}^M(k_1, k_2, \mu_{12}) \equiv \int d\omega_{k_1} d\theta_{k_1} B_s(\mathbf{k}_1, \mathbf{k}_2) Y_L^M(\omega_{k_1}, \theta_{k_1}). \quad (\text{A.9})$$

Restricting to the monopole $L = 0$ and expanding the internal angle $\mu_{12} \equiv \hat{\mathbf{k}}_1 \cdot \hat{\mathbf{k}}_2$ in Legendre polynomials,

$$B_{s,0}(k_1, k_2; \mu_{12}) = \sum_{\ell=0}^{\ell_{\text{max}}} B_{s,0,\ell}(k_1, k_2) \mathcal{L}_\ell(\mu_{12}), \quad (\text{A.10})$$

with

$$B_{s,0,\ell}(k_1, k_2) \equiv \frac{2\ell+1}{2} \int_{-1}^1 d\mu_{12} B_{s,0}(k_1, k_2; \mu_{12}) \mathcal{L}_\ell(\mu_{12}), \quad (\text{A.11})$$

and k_3 fixed by triangle closure; we use $\ell_{\text{max}} = 10$.

3PCF. The analogous decomposition in configuration space proceeds identically. The 3PCF is first expanded in spherical harmonics with respect to the orientation of \mathbf{r}_{12} relative to $\hat{\mathbf{n}}$,

$$\zeta_s(\mathbf{r}_{12}, \mathbf{r}_{13}) = \sum_{L,M} \zeta_{s,L}^M(r_{12}, r_{13}, \mu_{12,13}) Y_L^M(\omega_{r_{12}}, \theta_{r_{12}}), \quad (\text{A.12})$$

where

$$\zeta_{s,L}^M(r_{12}, r_{13}, \mu_{12,13}) \equiv \int d\omega_{r_{12}} d\theta_{r_{12}} \zeta_s(\mathbf{r}_{12}, \mathbf{r}_{13}) Y_L^{M*}(\omega_{r_{12}}, \theta_{r_{12}}). \quad (\text{A.13})$$

Restricting to $L = 0$ and expanding the internal angle $\mu_{12,13} \equiv \hat{\mathbf{r}}_{12} \cdot \hat{\mathbf{r}}_{13}$ in Legendre polynomials,

$$\zeta_{s,0}(r_{12}, r_{13}; \mu_{12,13}) = \sum_{\ell=0}^{\ell_{\text{max}}} \zeta_{s,0,\ell}(r_{12}, r_{13}) \mathcal{L}_\ell(\mu_{12,13}), \quad (\text{A.14})$$

with

$$\zeta_{s,0,\ell}(r_{12}, r_{13}) \equiv \frac{2\ell+1}{2} \int_{-1}^1 d\mu_{12,13} \zeta_{s,0}(r_{12}, r_{13}; \mu_{12,13}) \mathcal{L}_\ell(\mu_{12,13}). \quad (\text{A.15})$$

For simplicity, in the following we refer to the multipoles of the isotropic component in redshift space as, respectively, B_ℓ and ζ_ℓ .

A.3. Redshift-space perturbation theory kernels

We collect here the explicit expressions for the redshift-space kernels Z_n that appear in the perturbative expansion of Eq. (3). These encode both the galaxy bias and the velocity field contributions to the galaxy density contrast in redshift space. The first-order kernel reads

$$Z_1(\mathbf{k}_1) = b_1 + f\mu_1^2, \quad (\text{A.16})$$

which reduces to the standard Kaiser factor (Kaiser 1987) when evaluated on the total wavevector, $Z_1(\mathbf{k}) = b_1 + f\mu^2$. The second-order kernel is

$$Z_2(\mathbf{k}_1, \mathbf{k}_2) = K_2(\mathbf{k}_1, \mathbf{k}_2) + f\mu^2 G_2(\mathbf{k}_1, \mathbf{k}_2) + \frac{f\mu k}{2} \left[\frac{\mu_1}{k_1} (b_1 + f\mu_2^2) + \frac{\mu_2}{k_2} (b_1 + f\mu_1^2) \right], \quad (\text{A.17})$$

where $\mu \equiv \hat{\mathbf{n}} \cdot \hat{\mathbf{k}}$ with $\mathbf{k} = \mathbf{k}_1 + \mathbf{k}_2$, $\mu_i \equiv \hat{\mathbf{n}} \cdot \hat{\mathbf{k}}_i$, and $k \equiv |\mathbf{k}_1 + \mathbf{k}_2|$. The bias kernel K_2 and the velocity kernel G_2 are defined as

$$K_2(\mathbf{k}_1, \mathbf{k}_2) = \frac{b_2}{2} + b_1 F_2(\mathbf{k}_1, \mathbf{k}_2) + b_{G_2} S(\mathbf{k}_1, \mathbf{k}_2), \quad (\text{A.18})$$

$$G_2(\mathbf{k}_1, \mathbf{k}_2) = G_2^{\text{PT}}(\mathbf{k}_1, \mathbf{k}_2), \quad (\text{A.19})$$

where F_2 and G_2 are the standard SPT density and velocity kernels, $S(\mathbf{k}_1, \mathbf{k}_2) \equiv (\hat{\mathbf{k}}_1 \cdot \hat{\mathbf{k}}_2)^2 - 1/3$ is the tidal shear invariant, and b_{G_2} is the non-local bias parameter associated with \mathcal{G}_2 . The third-order kernel, which enters the one-loop power spectrum and must be fully symmetrised over its arguments, reads

$$\begin{aligned} Z_3(\mathbf{k}_1, \mathbf{k}_2, \mathbf{k}_3) &= K_3(\mathbf{k}_1, \mathbf{k}_2, \mathbf{k}_3) \\ &+ f\mu^2 G_3(\mathbf{k}_1, \mathbf{k}_2, \mathbf{k}_3) + \frac{f^2 \mu^2 k^2}{2} (b_1 + f\mu_1^2) \frac{\mu_2 \mu_3}{k_2 k_3} \\ &+ f\mu k \frac{\mu_3}{k_3} \left[b_1 F_2(\mathbf{k}_1, \mathbf{k}_2) + f\mu_{12}^2 G_2(\mathbf{k}_1, \mathbf{k}_2) \right] \\ &+ f\mu k (b_1 + f\mu_1^2) \frac{\mu_{23}}{k_{23}} G_2(\mathbf{k}_2, \mathbf{k}_3) \\ &+ \frac{b_2}{2} f\mu k \frac{\mu_1}{k_1} + b_{G_2} f\mu k \frac{\mu_1}{k_1} S(\mathbf{k}_2, \mathbf{k}_3), \end{aligned} \quad (\text{A.20})$$

where $\mathbf{k} = \mathbf{k}_1 + \mathbf{k}_2 + \mathbf{k}_3$, $\mu \equiv \hat{\mathbf{n}} \cdot \hat{\mathbf{k}}$, $k_{ij} \equiv |\mathbf{k}_i + \mathbf{k}_j|$ and $\mu_{ij} \equiv \hat{\mathbf{n}} \cdot (\mathbf{k}_i + \mathbf{k}_j)/k_{ij}$. The third-order bias kernel is

$$K_3(\mathbf{k}_1, \mathbf{k}_2, \mathbf{k}_3) = b_1 F_3(\mathbf{k}_1, \mathbf{k}_2, \mathbf{k}_3) + b_2 F_2(\mathbf{k}_1, \mathbf{k}_2) \\ + b_{G_2} [G_2(\mathbf{k}_1, \mathbf{k}_2) + F_2(\mathbf{k}_1, \mathbf{k}_2) S(\mathbf{k}_1 + \mathbf{k}_2, \mathbf{k}_3)] \\ + b_{\Gamma_3} \gamma_3(\mathbf{k}_1, \mathbf{k}_2, \mathbf{k}_3), \quad (\text{A.21})$$

where F_3 is the third-order SPT density kernel, G_3 is the corresponding velocity kernel, and γ_3 is the third-order tidal operator associated with the bias parameter b_{Γ_3} . The full Z_3 kernel is obtained by summing over all $3! = 6$ permutations of $(\mathbf{k}_1, \mathbf{k}_2, \mathbf{k}_3)$ and dividing by 6.

Appendix B: Clustering estimators and measurements

B.1. Clustering estimators

In what follows we describe the 2PCF and 3PCF estimators adopted, the harmonic decompositions employed, and the specific choices made for the data and mock analyses. Throughout this work we adopt the plane-parallel approximation. For the 2PCF, the line of sight (LOS) is defined for each pair of galaxies as the direction of its midpoint. For the 3PCF, we do not consider any explicit LOS dependence, since we consider only the LOS-averaged statistic. Both estimators belong to the class of Szapudi–Szalay estimators (Szapudi & Szalay 1998), which provide unbiased, minimum-variance counts for N -point statistics and naturally account for boundary and selection effects through the inclusion of random catalogues; in compact form, they can be written as $(D - R)^N/R^N$.

B.1.1. Two-point correlation function

We estimate the anisotropic 2PCF using the Landy–Szalay estimator (Landy & Szalay 1993),

$$\tilde{\xi}(s, \mu) = \frac{DD(s, \mu) - 2DR(s, \mu) + RR(s, \mu)}{RR(s, \mu)}, \quad (\text{B.1})$$

where $DD(s, \mu)$, $DR(s, \mu)$ and $RR(s, \mu)$ are the normalised counts of data–data, data–random and random–random pairs in bins of separation s and cosine angle $\mu = \hat{\mathbf{s}} \cdot \hat{\mathbf{n}}$ with respect to the LOS $\hat{\mathbf{n}}$. The estimator is applied independently to each of the four BOSS data chunks, and identically to each mock realisation. Each pair count is weighted by the product of the total weights w_{tot} of the two objects.

We compress the anisotropic 2PCF by projecting onto Legendre polynomials,

$$\tilde{\xi}_\ell(s) = \frac{2\ell + 1}{2} \int_{-1}^1 d\mu \tilde{\xi}(s, \mu) \mathcal{L}_\ell(\mu), \quad (\text{B.2})$$

and retain the monopole ($\ell = 0$), quadrupole ($\ell = 2$) and hexadecapole ($\ell = 4$). The adopted binning is $\Delta s = 5 h^{-1} \text{Mpc}$ in separation and $\Delta\mu = 0.01$ for the cosine angle, with measurements reported at bin centres. The scales used in the cosmological analysis are $s \in [30, 130] h^{-1} \text{Mpc}$, discussed further in Sec. 4.3.

B.1.2. Three-point correlation function

The 3PCF can be estimated using the unbiased, minimum-variance Szapudi & Szalay (1998) estimator,

$$\tilde{\xi}(\mathbf{x}_1, \mathbf{x}_2, \mathbf{x}_3) = \frac{DDD - 3DDR + 3DRR - RRR}{RRR}, \quad (\text{B.3})$$

where DDD , DDR , DRR , and RRR denote the normalised triplet counts with zero, one, two, and three random points, respectively. This estimator automatically subtracts the disconnected part of the three-point statistics and accounts for boundary and selection effects through the inclusion of the random catalogue, making it well suited for a masked survey such as BOSS DR12. As for the 2PCF, the estimator is applied identically to each mock catalogue, using the associated random catalogue.

The brute-force evaluation of Eq. (B.3) scales as $O(N^3)$ with the number of objects N , making it prohibitive for samples of the size of BOSS DR12. To reduce the computational cost, we use the MEASCORR code (Farina et al. 2026; Euclid Collaboration: Guidi et al. 2026; Euclid Collaboration: Veropalumbo et al. 2026), which implements the Spherical Harmonic Decomposition (SHD) algorithm presented in Slepian & Eisenstein (2015, 2018), achieving $O(N^2)$ scaling. The speed-up of the SHD algorithm is achieved by noting that, centred on each galaxy \mathbf{x} , the radially binned density field can be expanded in spherical harmonics,

$$a_{\ell m}(r; \mathbf{x}) = \int d\Omega \bar{\delta}(r, \hat{\mathbf{r}}; \mathbf{x}) Y_{\ell m}^*(\hat{\mathbf{r}}), \quad (\text{B.4})$$

where $\bar{\delta}(r, \hat{\mathbf{r}}; \mathbf{x})$ is the density field radially binned in the shell of radius r around the centre \mathbf{x} . Using the spherical-harmonic addition theorem, the Legendre polynomial of the opening angle between two side vectors $\hat{\mathbf{r}}_1$ and $\hat{\mathbf{r}}_2$ can be factored into a product of separately computed spherical-harmonic coefficients,

$$\mathcal{L}_\ell(\hat{\mathbf{r}}_1 \cdot \hat{\mathbf{r}}_2) = \frac{4\pi}{2\ell + 1} \sum_{m=-\ell}^{\ell} Y_{\ell m}(\hat{\mathbf{r}}_1) Y_{\ell m}^*(\hat{\mathbf{r}}_2). \quad (\text{B.5})$$

The local estimate of the ℓ -th multipole of the 3PCF about the centre \mathbf{x} therefore becomes

$$\hat{\xi}_\ell^{\text{loc}}(r_1, r_2; \mathbf{x}) = \frac{\delta(\mathbf{x})}{4\pi} \sum_{m=-\ell}^{\ell} a_{\ell m}(r_1; \mathbf{x}) a_{\ell m}^*(r_2; \mathbf{x}), \quad (\text{B.6})$$

and the global multipole coefficient is obtained by averaging over all galaxies acting as centres,

$$\bar{\xi}_\ell(r_1, r_2) = \frac{1}{N} \sum_{\mathbf{x} \in \text{gal}} \hat{\xi}_\ell^{\text{loc}}(r_1, r_2; \mathbf{x}). \quad (\text{B.7})$$

At any given centre, the $a_{\ell m}$ coefficients are precomputed once for each radial bin, so no $O(N^2)$ operation per centre is ever required; the scaling reduces to $O(N \times nV_{R_{\text{max}}})$, i.e. $O(N^2)$ overall, with the same favorable scaling as the two-point estimator.

In this work we focus on the isotropic component of the 3PCF with respect to the line of sight, i.e. we consider only the monopole with respect to the LOS, which is equivalent to averaging the 3PCF over all orientations of the triangle with respect to the LOS. The full LOS-anisotropic 3PCF is left for future work. We retain multipoles up to $\ell_{\text{max}} = 4$, which capture the bulk of the cosmological constraining power of the 3PCF while keeping the data-vector dimension manageable. Including higher multipoles would in principle add information, but at the cost of inflating the data vector, degrading the conditioning of the joint covariance matrix and thereby reducing the stability of its inversion and the reliability of the resulting parameter inference. The choice $\ell_{\text{max}} = 4$ therefore represents a principled optimum between information content and numerical stability of the likelihood analysis.

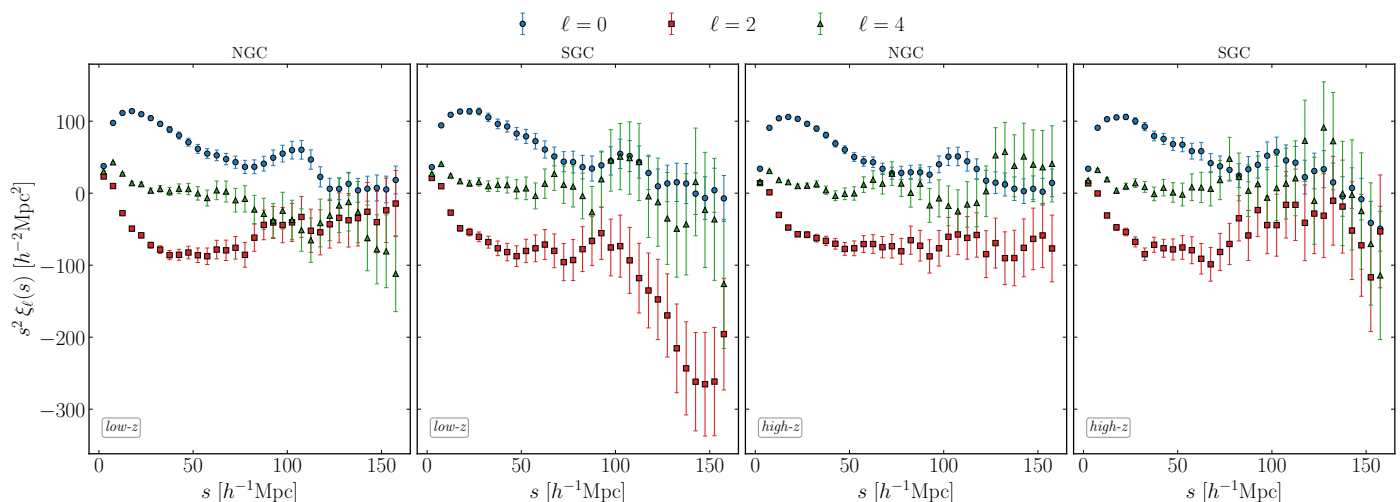


Fig. B.1: Multipoles of the two-point correlation function measured from the four BOSS DR12 data chunks. Each panel shows $s^2 \xi_\ell(s)$ as a function of separation s , for the monopole ($\ell = 0$, blue), quadrupole ($\ell = 2$, orange) and hexadecapole ($\ell = 4$, green). Columns correspond to the two sky regions (NGC, left; SGC, right), while rows correspond to the two redshift bins (*low-z* with $z_{\text{eff}} \approx 0.32$, top; *high-z* with $z_{\text{eff}} \approx 0.57$, bottom). Measurements are performed in the range $s \in [0, 150] h^{-1} \text{Mpc}$ with bin width $\Delta s = 5 h^{-1} \text{Mpc}$; bin centres are located at $s = 2.5, 7.5, \dots, 147.5 h^{-1} \text{Mpc}$. Error bars are the square root of the diagonal of the 2PCF covariance matrix $\hat{C}_{\xi\xi}$, estimated from the 2048 MultiDark-Patchy mock catalogues.

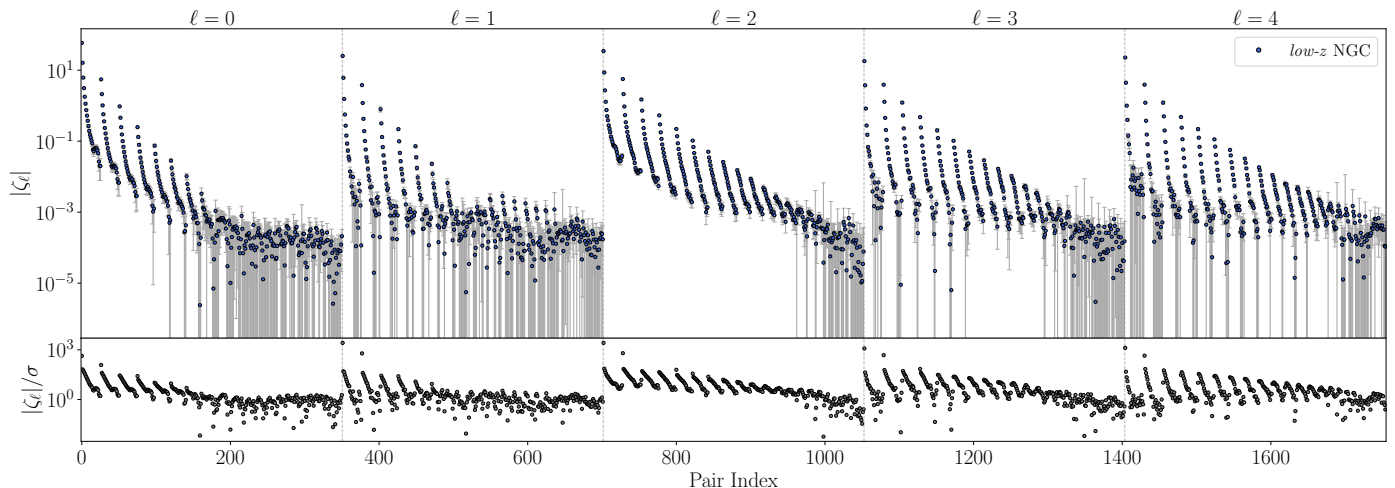


Fig. B.2: Multipoles of the three-point correlation function measured from the NGC-*low-z* chunk of BOSS DR12 ($z_{\text{eff}} \approx 0.32$), shown as a function of the ordered pair index (r_1, r_2) with $r_1 \leq r_2$. Triangles are measured over the range $r_{1,2} \in [0, 150] h^{-1} \text{Mpc}$ with bin width $\Delta r = 5 h^{-1} \text{Mpc}$; pairs are sorted in ascending order of r_1 and then r_2 . *Top panel*: measured multipoles $\zeta_\ell(r_1, r_2)$ for $\ell = 0, 1, 2, 3, 4$; grey error bars are the square root of the diagonal of $\hat{C}_{\zeta\zeta}$, estimated from the 2048 Patchy mocks. *Bottom panel*: absolute signal-to-noise ratio $|\zeta_\ell(r_1, r_2)|/\sigma_{\zeta_\ell(r_1, r_2)}$ for each multipole and configuration.

B.2. Clustering measurements

We present here the measurements of the 2PCF and 3PCF extracted from the four BOSS DR12 data chunks (NGC/SGC \times *low-z/high-z*) using the estimators described in Sec. B.1. In both cases, error bars on individual data points represent the square root of the diagonal of the respective covariance matrix block, estimated from the full suite of 2048 MultiDark-Patchy mock catalogues as described in Sec. 4.1. The fiducial cosmological parameters of the mock catalogues, used to convert angles and redshifts into comoving coordinates, are listed in Tab. B.1.

B.2.1. 2PCF measurements

The anisotropic 2PCF $\tilde{\xi}(s, \mu)$ is measured for each of the four data chunks using the Landy–Szalay estimator of Eq. (B.1). We bin pair separations over the range $s \in [0, 150] h^{-1} \text{Mpc}$ with a fixed bin width of $\Delta s = 5 h^{-1} \text{Mpc}$, yielding 30 bins with centres at $s = 2.5, 7.5, \dots, 147.5 h^{-1} \text{Mpc}$. The anisotropic signal is then compressed into the monopole ($\ell = 0$), quadrupole ($\ell = 2$) and hexadecapole ($\ell = 4$) multipole moments via Eq. (B.2).

The resulting measurements, multiplied by s^2 to enhance the visibility of the clustering signal, are shown in Fig. B.1 for all four chunks. The monopole is detected with high signal-to-noise across the full separation range, and shows the characteristic bump at $s \sim 100 h^{-1} \text{Mpc}$ associated with the baryon acous-

Table B.1: Fiducial cosmological parameters of the MultiDark-Patchy mock catalogues (Kitaura et al. 2016; Klypin et al. 2016).

Parameter	Value
Ω_m	0.307115
Ω_Λ	0.692885
Ω_b	0.048
σ_8	0.8288
h	0.6777
n_s	0.9611
A_s	2.106×10^{-9}
M_v	0
Ω_k	0

tic oscillation (BAO) feature. The measurements from the NGC and SGC regions are mutually consistent within the errors, as expected for a survey with homogeneous selection. The *high-z* sample shows a systematically larger clustering amplitude compared to *low-z*, reflecting the higher effective linear bias of the more massive galaxy population targeted by the CMASS selection at $z_{\text{eff}} \approx 0.57$.

B.2.2. 3PCF measurements

The 3PCF multipoles $\zeta_\ell(r_1, r_2)$ for $\ell = 0, 1, 2, 3, 4$ are measured for each data chunk using the MEASCORR package (Farina et al. 2026), which implements the SHD estimator described in App. B.1.2. The two side lengths are binned over the range $r_{1,2} \in [0, 150] h^{-1}\text{Mpc}$ with $\Delta r = 5 h^{-1}\text{Mpc}$, yielding bin centres at 2.5, 7.5, ..., 147.5 $h^{-1}\text{Mpc}$. Triangle configurations are parametrised by ordered pairs (r_1, r_2) with $r_1 \leq r_2$, avoiding double counting; the pairs are sorted first in ascending order of r_1 and then of r_2 , defining a unique Pair Index running over all $N_{\text{pairs}} = N_{\text{bins}}(N_{\text{bins}} + 1)/2$ configurations.

Figure B.2 shows the NGC measurements for the *low-z* bin; the SGC results are fully consistent and enter the analysis on equal footing. The monopole ($\ell = 0$) dominates in amplitude across the full range of configurations, while the higher multipoles ($\ell = 1, 2, 3, 4$) are detected with $|\zeta_\ell|/\sigma > 1$ over a significant fraction of configurations at small scales. At large separations all multipoles fall below the noise level, confirming that the effective information content of the 3PCF is dominated by the small-scale configurations retained in the data vector.

Appendix C: Dependence of the 2PCF inference on the minimum scale cut

This appendix explores the dependence of the cosmological inference on the minimum scale cut r_{min} , varying between 20 and 80 $h^{-1}\text{Mpc}$. The goal is to assess the stability of the posterior distributions and the goodness of fit as progressively smaller scales are included in the analysis.

Table C.1 reports the data-vector size N_d , the number of degrees of freedom $N_{\text{dof}} = N_d - N_p$, and the Hartlap and Percival correction factors as a function of r_{min} . Since $N_m = 2048 \gg N_d$ across all scale cuts, the Hartlap correction remains within $\lesssim 3\%$ of unity, while the Percival correction amounts to at most $\sim 12\%$ at $r_{\text{min}} = 20 h^{-1}\text{Mpc}$, decreasing to $\sim 4\%$ at $r_{\text{min}} = 80 h^{-1}\text{Mpc}$. Both corrections are properly accounted for in the likelihood evaluation.

Table C.1: Data-vector size and covariance correction factors for the 2PCF-only analysis as a function of r_{min} , with $r_{\text{max}} = 130 h^{-1}\text{Mpc}$ fixed. N_d is the number of data points, $N_{\text{dof}} = N_d - N_p$ the degrees of freedom, and α_H , α_P the Hartlap and Percival correction factors (Eqs. 31–33).

$r_{\text{min}} [h^{-1}\text{Mpc}]$	N_d	α_H	α_P	N_{dof}
20	264	0.9711	1.1249	245
30	240	0.9734	1.1101	221
40	216	0.9761	1.0957	197
50	192	0.9784	1.0817	173
60	168	0.9812	1.0680	149
70	144	0.9839	1.0547	125
80	120	0.9863	1.0416	101

Cosmological parameters. Figure C.1 shows the dependence of the marginalised posterior means and 68% credible intervals of $10^9 A_s$, h , and ω_{cdm} as a function of r_{min} for the *low-z*, *high-z*, and *combined* analyses.

The Hubble parameter h is remarkably stable across the full range of scale cuts, with no evidence of a significant trend and excellent agreement between the two redshift bins at all values of r_{min} . The scalar amplitude $10^9 A_s$ shows a mild dependence on r_{min} , with a gradual increase in its posterior mean and a corresponding broadening of its uncertainty as smaller scales are progressively removed from the analysis. This behaviour reflects the loss of small-scale information that contributes to constraining the overall amplitude of matter fluctuations. The cold dark matter density ω_{cdm} exhibits a more pronounced dependence on r_{min} , with systematically lower values favoured when smaller scales are included. This trend is consistent with an evolving degeneracy between A_s and ω_{cdm} as broad-band shape information is progressively added or removed from the data vector. The *low-z* and *high-z* samples remain broadly consistent across the full range of scale cuts, with differences typically at the $\sim 1\text{--}2\sigma$ level at most.

Nuisance parameters. Figure C.2 shows the corresponding behaviour of the nuisance parameters as a function of r_{min} . The linear bias b_1 and velocity dispersion parameter a_{vir} are stable across all scale cuts and for both redshift bins, indicating robustness with respect to the choice of minimum scale. In contrast, the EFT counterterms c_0 and c_2 exhibit a smooth dependence on r_{min} , with larger absolute values when smaller scales are included in the analysis. This reflects their role in absorbing residual non-linear contributions rather than indicating any breakdown of the perturbative model. The higher-order bias parameters remain consistent with zero within uncertainties for all scale cuts considered.

However, the goodness of fit, quantified via the χ^2 statistic, as shown in Fig. 2), remains statistically acceptable across the entire range of scale cuts considered. No significant degradation of the fit is observed when including smaller scales down to $r_{\text{min}} = 20 h^{-1}\text{Mpc}$, indicating that the model provides a consistent description of the data within the explored range. Overall, the dependence of both cosmological and nuisance parameters on r_{min} is smooth and well-behaved, with no indication of a sharp transition in the validity of the model. In the absence of statistically significant degradation in the χ^2 statistic, we adopt $r_{\text{min}} = 20 h^{-1}\text{Mpc}$ as the fiducial choice for the baseline analysis, as it maximises the available information content while remaining fully consistent with the goodness-of-fit criterion.

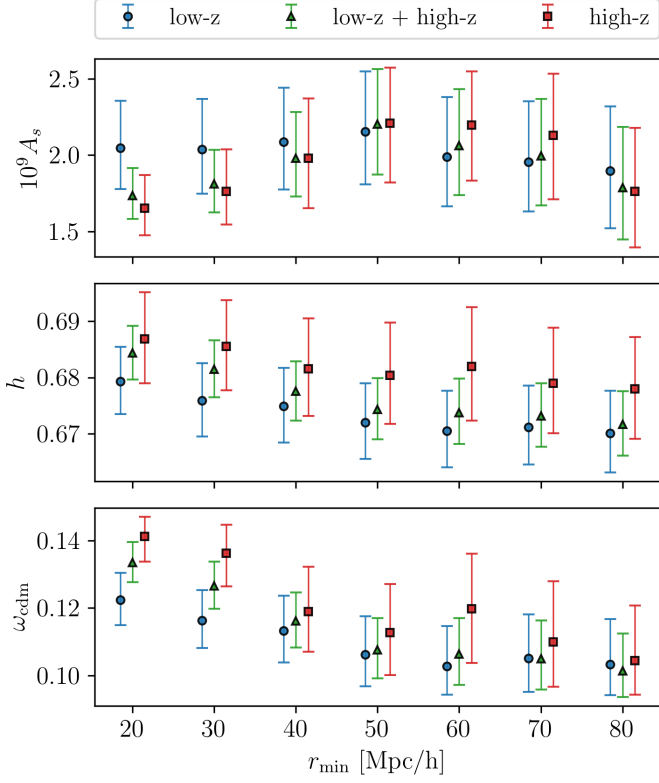


Fig. C.1: Marginalised posterior means and 68% credible intervals for $10^9 A_s$ (top), h (middle), and ω_{cdm} (bottom) as a function of the minimum fitting scale r_{min} for the *low-z* (blue circles), *high-z* (red squares), and *combined* (green triangles) 2PCF analyses. The grey dashed horizontal line marks the fiducial value of each parameter.

Appendix D: Scale cut and posterior validation for the joint analysis

We present here the supporting diagnostics for the joint 2PCF+3PCF analysis of Sect. 5.2, complementing the cosmological parameter running and goodness-of-fit discussed in the main text with the behaviour of the nuisance parameters and the full posterior distributions. Also table D.1 reports, for each combination of $r_{\text{min}}^{\text{3PCF}}$ and η_{min} , the total size of the joint data vector N_d , the number of degrees of freedom $N_{\text{dof}} = N_d - N_p$ with $N_p = 19$, and the Hartlap and Percival correction factors (Eqs. 31–33), with $r_{\text{min}}^{\text{2PCF}} = 20 h^{-1} \text{Mpc}$ fixed throughout. Unlike the 2PCF-only case, where both corrections are negligible ($\lesssim 0.6\%$), the ratio N_d/N_m is non-negligible across all joint configurations: the Hartlap correction reduces the effective precision matrix by up to $\sim 22\%$ at the smallest scale cut, while the Percival correction inflates the marginalised parameter variances by up to $\sim 25\%$. Both corrections decrease monotonically as $r_{\text{min}}^{\text{3PCF}}$ increases and as η_{min} increases, reflecting the progressive reduction of the data-vector size.

Nuisance parameter stability

Figure D.1 shows the marginalised posterior means and 68% credible intervals for the nuisance parameters of both redshift bins as a function of $r_{\text{min}}^{\text{3PCF}}$, for the three elongation cuts $\eta_{\text{min}} \in \{1, 2, 3\}$.

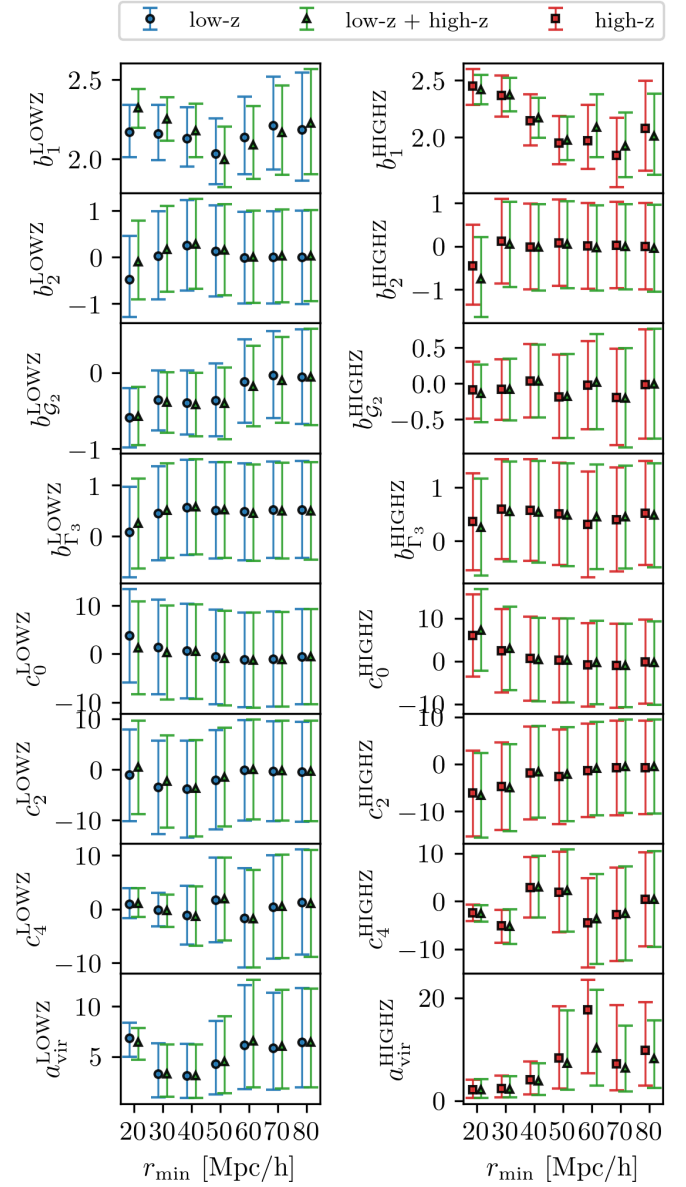


Fig. C.2: Marginalised posterior means and 68% credible intervals for the nuisance parameters as a function of r_{min} , for the *low-z* bin (left column, blue circles) and the *high-z* bin (right column, red squares); green triangles show the corresponding results from the *combined* analysis.

The linear bias b_1 is stable across the entire range of $r_{\text{min}}^{\text{3PCF}}$ for both redshift bins and all elongation cuts, with no appreciable systematic trend, confirming that this parameter is robustly constrained independently of the 3PCF scale cut. The velocity-dispersion parameter a_{vir} shows a notable anomaly at $r_{\text{min}}^{\text{3PCF}} = 40 h^{-1} \text{Mpc}$ for $\eta_{\text{min}} = 1$, where it drops to near-zero values: this signals that nearly-degenerate triangle configurations, admitted by the loose elongation cut, introduce squeezed configurations in which the FoG damping is poorly constrained by the data. This pathological behaviour disappears for $\eta_{\text{min}} \geq 2$ and vanishes entirely for all η_{min} from $r_{\text{min}}^{\text{3PCF}} \simeq 50 h^{-1} \text{Mpc}$ onward, providing an independent motivation for the choice $\eta_{\text{min}} = 3$ as the reference elongation cut.

The EFT counterterms c_0 and c_2 exhibit enhanced scatter and systematically large absolute values at $r_{\text{min}}^{\text{3PCF}} \leq 45 h^{-1} \text{Mpc}$, most

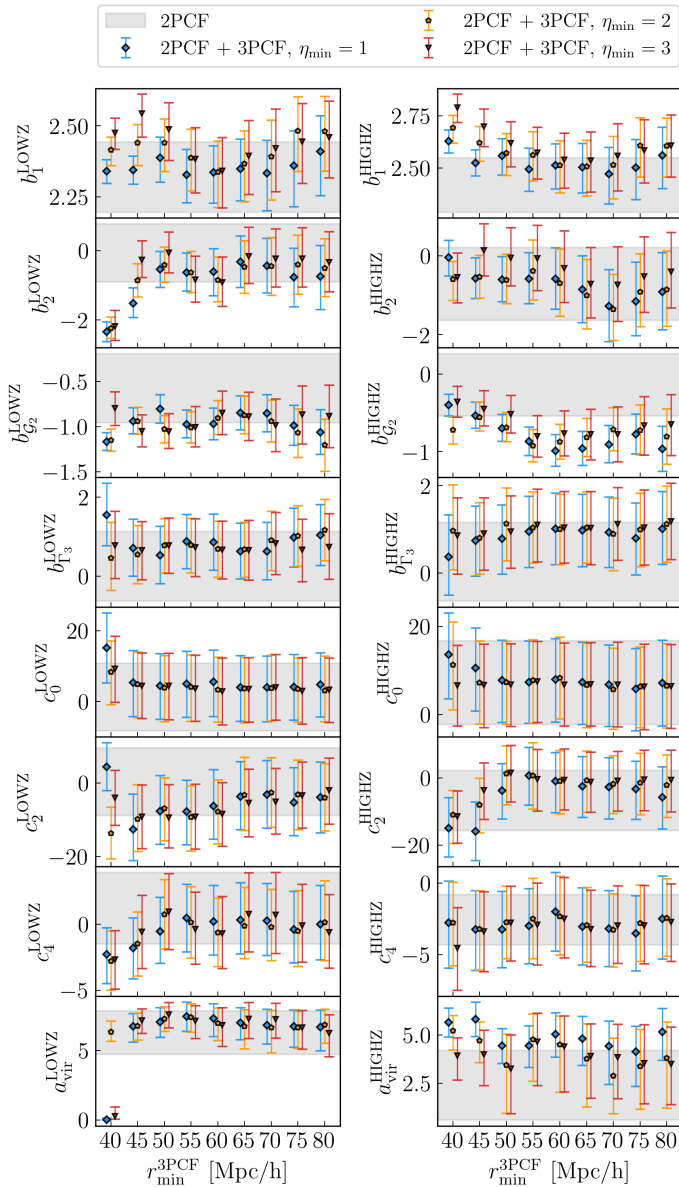


Fig. D.1: Marginalised posterior means and 68% credible intervals for the nuisance parameters of the joint 2PCF+3PCF *combined* analysis as a function of $r_{\min}^{3\text{PCF}}$, for the *low-z* (left column) and *high-z* (right column) bins. Symbols as in Fig. 5: blue diamonds ($\eta_{\min} = 1$), green pentagons ($\eta_{\min} = 2$), orange triangles ($\eta_{\min} = 3$).

pronounced for $\eta_{\min} = 1$. This behaviour mirrors the instability seen in the cosmological parameters at the same scale cuts (Fig. 5) and is consistent with the EFT counterterms absorbing non-perturbative small-scale contributions beyond the range of validity of the model. From $r_{\min}^{3\text{PCF}} \simeq 55 h^{-1}\text{Mpc}$ all three elongation cuts yield counterterm values consistent with perturbative expectations, with no residual trend. The higher-order bias parameters b_2 , b_{G_2} , b_{Γ_3} and c_4 are consistent with zero within their uncertainties throughout, with no significant dependence on $r_{\min}^{3\text{PCF}}$ or η_{\min} .

Taken together with the χ_{red}^2 criterion (Fig. 4) and the cosmological parameter running (Fig. 5), the nuisance parameter behaviour consistently identifies $r_{\min}^{3\text{PCF}} = 60 h^{-1}\text{Mpc}$ and $\eta_{\min} =$

Table D.1: Joint data-vector size and covariance correction factors as a function of $r_{\min}^{3\text{PCF}}$ and η_{\min} , with $r_{\min}^{2\text{PCF}} = 20 h^{-1}\text{Mpc}$ fixed. N_d is the total number of data points in the original joint 2PCF+3PCF vector, N_{SV}^* the number of modes retained after covariance compression, $N_{\text{dof}} = N_{\text{SV}}^* - N_p$ the degrees of freedom with $N_p = 19$, and α_H , α_P the Hartlap and Percival correction factors (Eqs. 31–33).

$r_{\min}^{3\text{PCF}} [h^{-1}\text{Mpc}]$	η_{\min}	N_d	N_{SV}^*	α_H	α_P	N_{dof}
30	1	3304	433	0.7829	1.2487	414
30	2	3000	393	0.8029	1.2180	374
30	3	2712	366	0.8164	1.1981	347
35	1	3000	396	0.8014	1.2202	377
35	2	2712	358	0.8204	1.1923	339
35	3	2440	333	0.8329	1.1746	314
40	1	2712	360	0.8194	1.1937	341
40	2	2440	326	0.8364	1.1697	307
40	3	2184	304	0.8474	1.1547	285
45	1	2440	331	0.8339	1.1732	312
45	2	2184	301	0.8489	1.1527	282
45	3	1944	280	0.8594	1.1387	261
50	1	2184	304	0.8474	1.1547	285
50	2	1944	279	0.8599	1.1381	260
50	3	1720	260	0.8694	1.1258	241
55	1	1944	286	0.8564	1.1427	267
55	2	1720	261	0.8689	1.1264	242
55	3	1512	244	0.8774	1.1156	225
60	1	1720	270	0.8644	1.1322	251
60	2	1512	244	0.8774	1.1156	225
60	3	1320	227	0.8859	1.1050	208
65	1	1512	256	0.8714	1.1232	237
65	2	1320	230	0.8844	1.1069	211
65	3	1144	216	0.8914	1.0983	197
70	1	1320	244	0.8774	1.1156	225
70	2	1144	219	0.8899	1.1001	200
70	3	984	204	0.8974	1.0910	185
75	1	1144	232	0.8834	1.1081	213
75	2	984	208	0.8954	1.0934	189
75	3	840	193	0.9030	1.0844	174
80	1	984	222	0.8884	1.1019	203
80	2	840	196	0.9015	1.0862	177
80	3	712	182	0.9085	1.0779	163

3 as the conservative threshold below which the perturbative model cannot be considered reliable.

Full posterior distributions

Figure D.2 shows the complete marginalised posterior distributions for the reference joint configuration ($r_{\min}^{3\text{PCF}} = 60 h^{-1}\text{Mpc}$, $\eta_{\min} = 1$), extending the three-parameter cosmological corner plot of Fig. 6 to include all nuisance parameters for both redshift bins.

Several inter-parameter correlations are visible in the full posterior. The well-known degeneracy between b_1 and $10^9 A_s$ is clearly present, as the two parameters jointly control the overall clustering amplitude; this degeneracy is partially broken by the broad-band shape information encoded in ω_{cdm} and h , with a residual negative correlation between $10^9 A_s$ and ω_{cdm} consistent with their joint sensitivity to the power spectrum shape. The nuisance parameters of the two redshift bins show no significant cross-bin correlations, validating the assumption of independent bias parameters in the combined analysis.

A comparison between the 2PCF-only and the joint 2PCF+3PCF posteriors reveals a systematic tightening of the

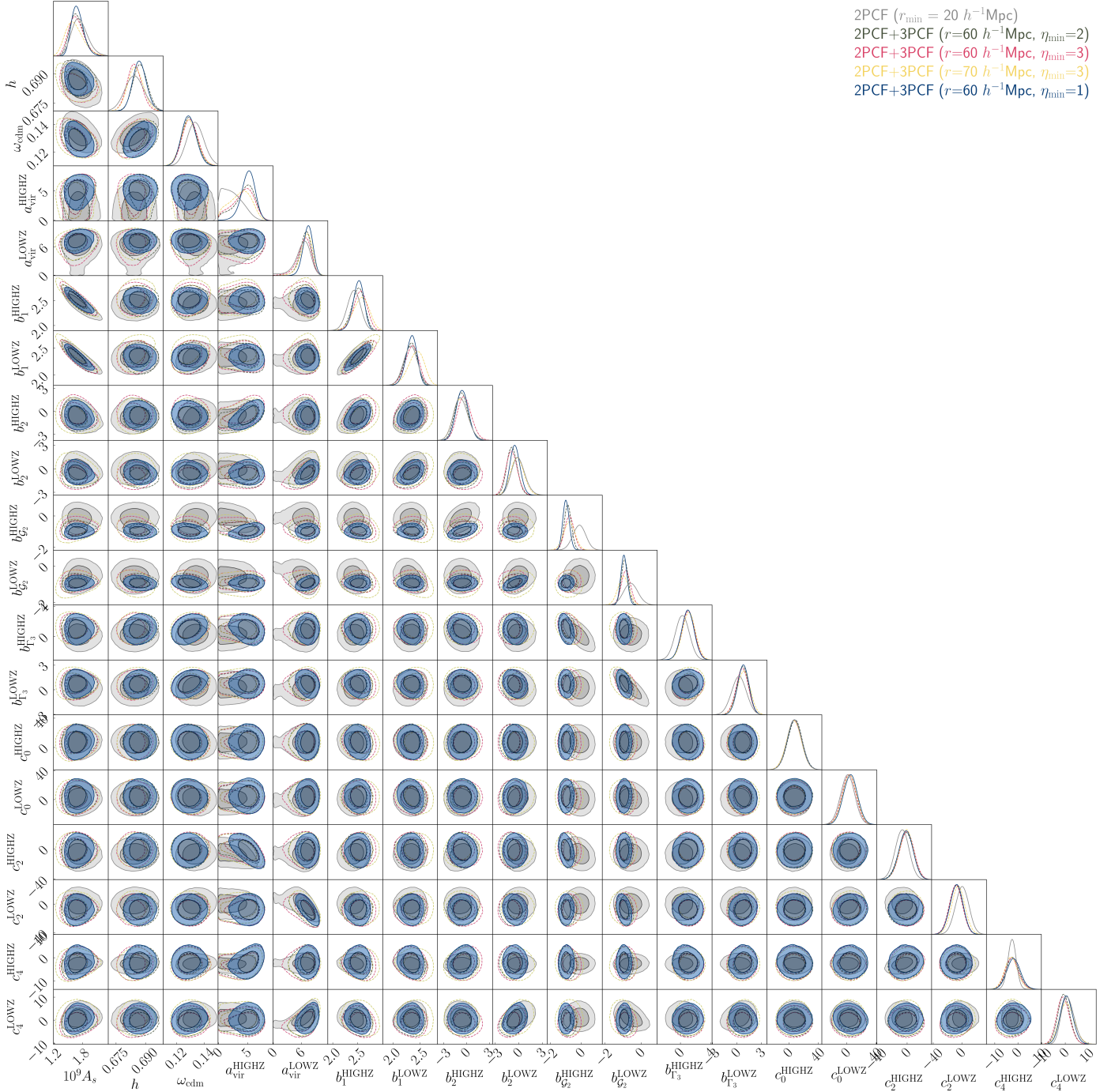


Fig. D.2: As in Fig. 6, but showing all the parameter set.

marginalised constraints across the full parameter space. Beyond the cosmological parameters discussed in Sect. 5.2, the improvement is most apparent in the linear bias parameters b_1^{LOWZ} and b_1^{HIGHZ} , reflecting the direct sensitivity of the 3PCF to the large-scale bias through its leading-order dependence on the squared density field. A tightening is also visible for b_2 and b_{g_2} , consistent with the 3PCF's constraining power on higher-order bias parameters. The constraints on a_{vir} shift slightly but remain fully consistent between the two analyses, suggesting that the 3PCF mildly breaks the degeneracy between the finger-of-God damping scale and the linear bias parameters through its sensitivity to the angular structure of triangle configurations along the line of

sight. We note that a_{vir} is additionally susceptible to prior volume effects arising from its degeneracies with b_1 and $10^9 A_s$; however, since this parameter does not enter the cosmological inference directly, its marginalised posterior is not a primary diagnostic of this analysis.